CHAPTER 6

SLIDING WEAR OF Cu-MoS_2, Cu-rGO and Cu-x wt. % rGO-MoS_2 COMPOSITES

This chapter starts with the results on metallographic and mechanical properties characterization of copper based composites containing rGO (2 wt. %), MoS_2 (2 wt.%) and rGO-MoS_2 (2 wt.%) and variable content of rGO-MoS_2 (0.5 wt. %, 1.0 wt.%, 1.5 wt. % and 2 wt. %). However, results on friction and wear behavior of composites are presented in two sections wherein, section one contains the results on the dry sliding friction and wear of Cu-2 wt. % rGO, Cu- 2 wt. % MoS_2 and Cu- 2 wt. % rGO-MoS_2 at a load of 6N and sliding speed of 0.5 m. s^{-1}. The results on tribological characteristics of copper based composite containing different (0.5, 1.0, 1.5 and 2.0 wt. %) amount of rGO-MoS_2 under different loads of 4, 6, 8 and 10 N and a speed of 0.5 $m.s^{-1}$ are presented in the second section. The results have also been discussed on the basis of the features seen on the worn surfaces of composites as well as the counterface body slid against them to develop a coherent understanding of the tribological performance of the composites and to reveal the prevailing mechanisms of wear.

6.1 RESULTS

6.1.1 CHARACTERIZATION OF COMPOSITES

Figures 6.1 (a through d) show the microstructures of pure copper (designated as PC) and copper based composites Cu-2 wt.% rGO, Cu-2 wt.% MoS_2 and Cu-2 wt.% rGO-MoS_2 designated as CG, CM and CGM, respectively. The SEM micrograph of pure

copper (PC) shown in Fig. 6.1 (a) does not exhibit any secondary phase. Figure 6.1 (b) shows both low and high magnification micrographs of Cu-2 wt. % rGO composite CG with low magnification micrograph shown in the inset depicting the agglomeration of rGO over the surface seen in the form of black spots marked with the help of white arrows in the micrograph. The scanning electron microscope (SEM) micrograph of Cu-2 wt. % MoS_2 composite CM shown in Fig. 6.1 (c) reveals the presence of some voids along with uniformly dispersed bright phase of MoS_2 (shown by white arrows) throughout the micrograph whereas the micrograph pertaining Cu-2 wt. % rGO-MoS_2 composite i.e. CGM shows the presence of two distinct regions i.e. rGO and MoS_2 rich regions in the matrix of copper. The dark region, richer in rGO phase has been indicated using black arrow and the light grey regions richer in MoS_2 have been indicated by white arrows.

Figures 6.2 (a through) illustrate the microstructure of composites reinforced with different amounts (0.5, 1.0. 1.5 and 2 wt. %) of rGO-MoS_2 hybrid in matrix of Copper and designated as CGM 0.5 (0.5 wt. % rGO-MoS_2), CGM 1.0 (1.0 wt. % rGO-MoS_2), CGM 1.5 (1.5 wt. % rGO-MoS_2) and CGM 2.0 (2.0 wt. % rGO-MoS_2) as examined under SEM. The microstructure of the composite CGM 0.5 (0.5 wt. % rGO-MoS_2) shown in Fig 6.2 (a) suggests the agglomeration of rGO-MoS_2 phase (indicated by white arrows) in the form of bright patches. The microstructure of composite CGM 1.0 (1.0 wt. % rGO-MoS_2) depicted in Fig. 6.2 (b) exhibits a relatively uniform dispersion of bright phase rGO-MoS_2, whereas the micrograph of composite CGM 1.5 (1.5 wt. % rGO-MoS_2) shown in Fig.6.2 (c) also reveals a relatively uniform microstructure but with excess of reinforced phase at surface. However, the micrograph corresponding to CGM 2.0 (2.0 wt. % rGO-MoS_2) shown in Fig. 6.2 (d) reflects a uniformly distributed bright phase over the surface with several regions containing excessive presence of rGO-MoS_2.

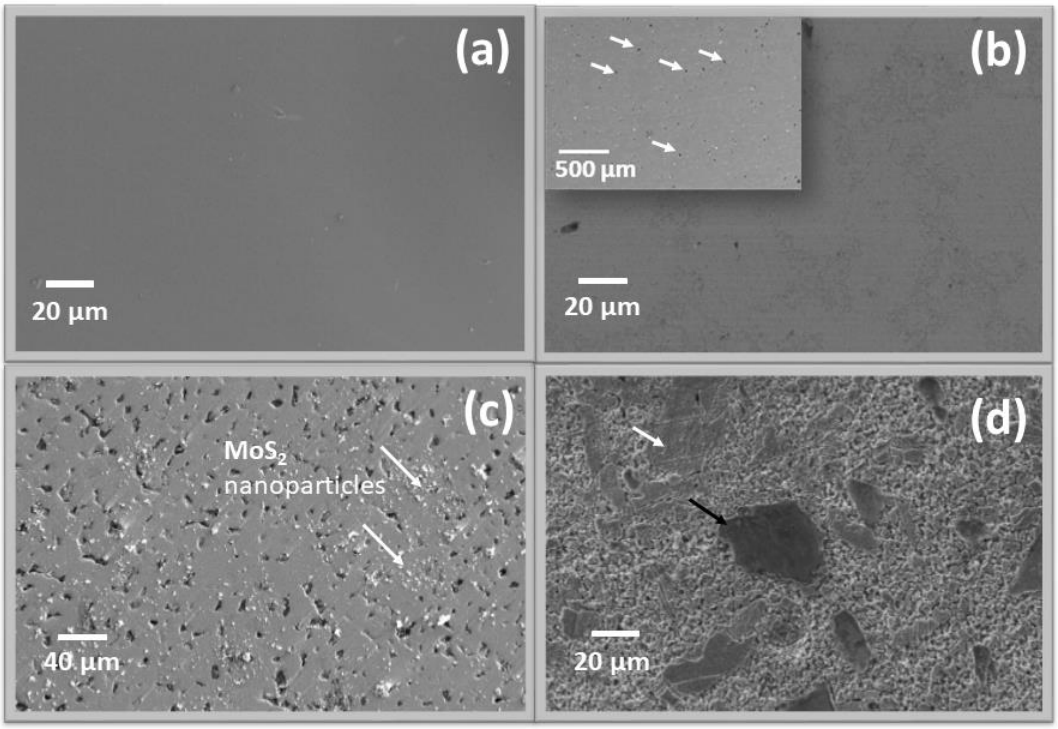

Fig. 6.1 SEM micrograph of (a) PC, (b) CG, (c) CM, (d) CGM. Inset of Figure b corresponds the low magnification image showing dark agglomerates.

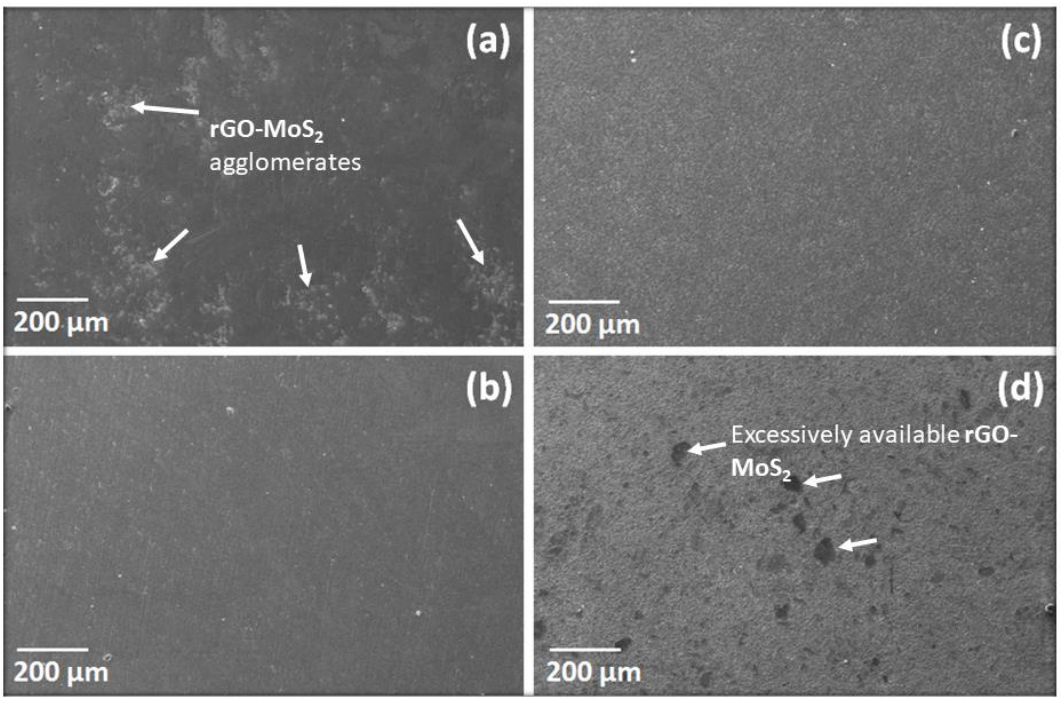

Fig. 6.2 SEM micrographs of (a) CGM 0.5, (b) CGM 1.0, (c) CGM 1.5 and (d) CGM 2.0 composites.

Figure 6.3 shows the X-Ray diffraction pattern for pure Cu (PC), Cu-2 wt. % rGO (CG), Cu-2 wt. % MoS_2 and Cu 2 wt. % rGO-MoS_2 (CGM) composites. All the composites and pure copper exhibit the sharp peaks at 2θ of 43.3 and 50.4° corresponding to (111) and (200) planes of copper respectively, (JCPDS card no. 85-1326). XRD pattern of CG composite exhibits a diffraction peak at 26.5° corresponding to the (002) plane of the reinforcing rGO phase, whereas, the XRD pattern of composite CM exhibits a very low intensity poor peak corresponding at 33.4° corresponding to the plane (101) of MoS_2. In order to have a better insight, X-ray diffraction pattern of CGM composite is expanded which reveals the presence of three distinct peaks for three different phases: 2θ of 26.5° for (002) plane of rGO, 33.4° corresponding to (101) plane of MoS_2 and 36.4° corresponding (111) plane of MoC as shown in the inset.

The XRD diffraction patterns of the composites containing different amounts (0.5, 1.0, 1.5 and 2.0 wt.%) of rGO-MoS_2 hybrid, namely, CGM0.5, CGM 1.0, CGM1.5 and CGM 2.0 illustrated in Fig. 6.4 reveals the crystalline features of Cu-rGO-MoS_2 composites. One may observe the presence of strong diffraction peaks at 2θ of 43.3°and 50.5° corresponding to (111) and (200) planes of copper (JCPDS card no. 851326) in diffraction patterns of all the composites as well as pure copper. In order to reveal the diffraction features of reinforced rGO-MoS_2 hybrid, the 2θ range of 24 to 38° has been expanded in the inset of the XRD patterns of all the composites as shown in Fig. 6.4. A diffraction peak at 2θ of 26.5° observed corresponding to (002) plane of graphene has confirms the presence of rGO-MoS_2 hybrid. The appearance of a peak at 2θ of 36.3° corresponds to (101) plane of MoC (JCPDS no.653494).

The density and hardness of spark plasma sintered pure Cu (PC), Cu-2 wt. % rGO (CG), Cu-2 wt. % MoS_2 and Cu 2 wt. % rGO-MoS_2 (CGM) composites along with their designations are given in Table 6. The density of the PC is found to be the highest

which is followed by the composite CGM, CG and CM as seen from Table 6.1. The incorporation of second phase in Cu matrix results in an increase in hardness of as evident from Table 6.1. The composite CGM has shown the highest value of Vickers hardness (75 HV), which was followed by CG (72 HV) and CM composite (70 HV).

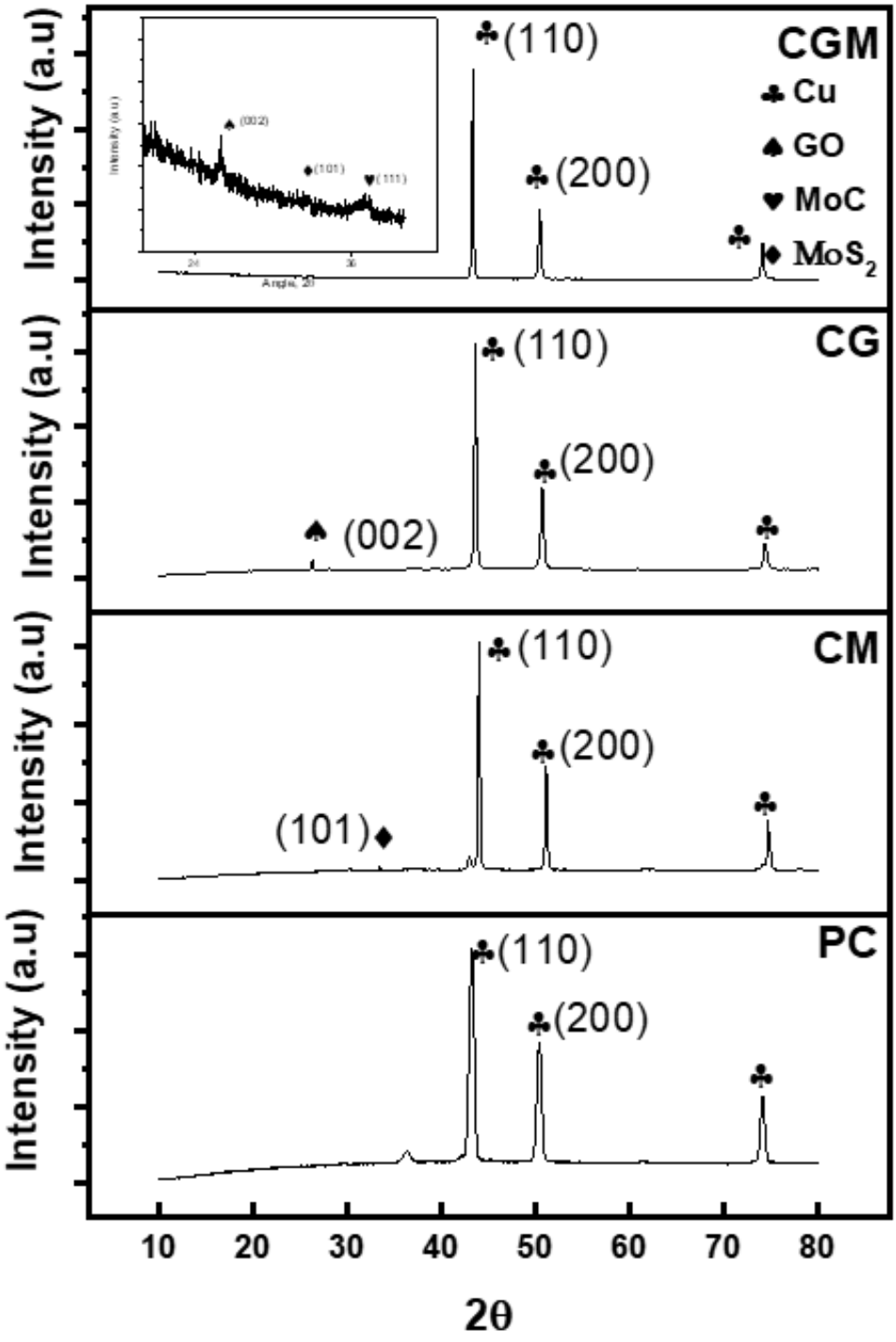

Fig. 6.3 XRD patterns of PC, CM, CG and CGM specimens.

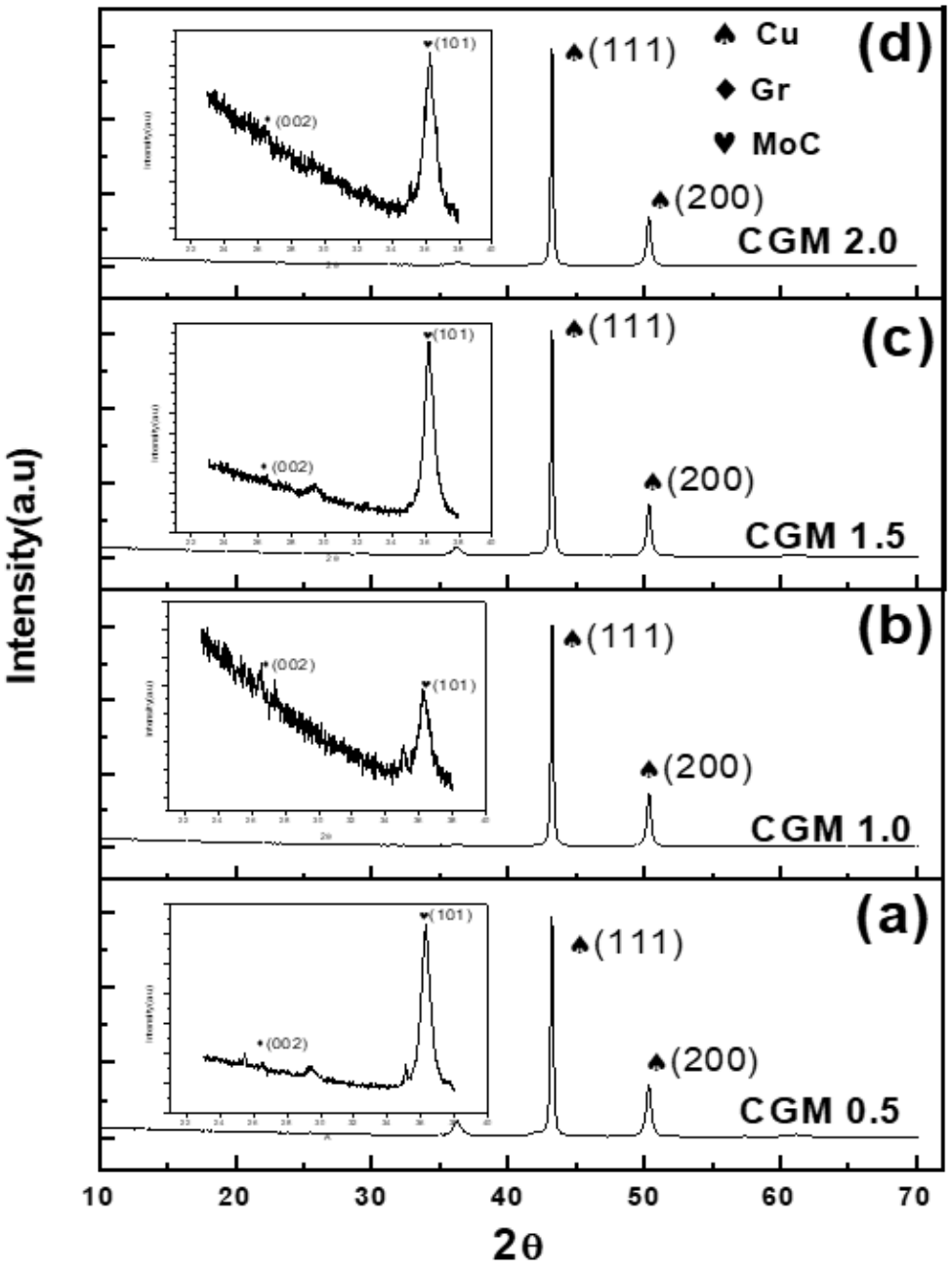

Fig. 6.4 XRD patters of CGM 0.5, CGM 1.0, CGM 1.5 and CGM 2.0.

Table 6.2 presents the density, hardness and designation of the composites containing different content (0.5, 1.0, 1.5 and 2.0 wt. %) of GO-MoS_2 hybrid. One may observe that both the density and the hardness increase with increasing content of rGO-MoS_2 up to 1 wt. % and decrease thereafter, till 2.0 wt. % addition. The composite containing 0.5 wt. % rGO-MoS_2 i.e. CGM 0.5 has Vickers hardness of 81 HV which increases on increasing the rGO-MoS_2 content up to 1 wt. % and reaches a value of 89

HV. Further increase in rGO-MoS_2 content results in a decrease in the hardness to a value of 76 HV for CGM1.5 and 74 HV for CGM 2.0.

Table 6.1 Composition, Designation**,** density and hardness of copper and composites

Composition	**Composition**	**Density, g.cm^{-3}**	**Hardness, HV$_{0.5}$**
Pure Cu	PC	8.71	63
Cu-2 wt.% rGO	CG	7.16	72
Cu-2 wt.% MoS_2	CM	6.95	70
Cu-2.0 wt.% rGO-MoS_2	CGM	7.44	75

Table 6.2 Composition, Designation**,** density and hardness of composites with containing different amount of rGO-MoS_2.

Composition	**Designation**	**Density, g.cm^{-3}**	**Hardness, HV$_{0.5}$**
Cu-0.5 wt.% rGO-MoS_2	CGM 0.5	7.0274	81
Cu-1.0 wt.% rGO-MoS_2	CGM 1.0	7.7705	89
Cu-1.5 wt.% rGO-MoS_2	CGM 1.5	7.1756	76
Cu-2.0 wt.% rGO-MoS_2	CGM 2.0	7.1013	74

6.1.2 FRICTION AND WEAR BEHAVIOR OF PURE Cu AND COMPOSITES (Cu-rGO, Cu-MoS_2 and Cu-rGO-MoS_2)

Figure 6.5 (a) shows the real time variation of coefficient of friction with number of cycles for PC, CG, CM and CGM whereas the variation of average coefficient of friction with composition is depicted in Fig. 6.b. One may observe an unstable variation of coefficient of friction with relatively larger amplitude of fluctuations for pure copper (PC) as compared to composites CG, CM and CGM as evident from Fig. 6.5 (a) A relatively stable and gradually increasing friction curve approaching the same value as of pure copper at 6000 cycles could be seen for composite CG, which appears to follow the

similar trend of variation like PC beyond 6000 cycles. The composite CM has shown a stable and sluggishly increasing curve with very small amplitude of fluctuations whereas a steady variation of coefficient of friction could be seen for composite CGM. The variation of average coefficient of friction with composition illustrated in Fig. 6 (b) shows that a significant reduction in coefficient of friction occurs with the addition of any of the three lubricants, namely, rGO, MoS_2 or rGO-MoS_2. It may further be observed that the largest reduction in coefficient of friction takes place by the addition of rGO-MoS_2 (0.08) hybrid and the smallest by the addition of rGO (0.47). The reduction caused by the addition of MoS_2 falls in-between (0.18). This reflects the effectiveness of rGO-MoS_2 hybrid in reducing the coefficient of friction in comparison to stand alone solid lubricants rGO or MoS_2 and reflects a possible synergetic action.

Figure 6.6 depicts the variation of wear rate with composition for PC and composites. One may observe a significant reduction in wear rate with the addition of the second phase i.e. rGO, or MoS_2 or rGO-MoS_2. The wear rate shown by pure Cu is the highest and that shown by the composite CGM containing 2 wt. % rGO-MoS_2 is the lowest. The wear rate of the composite Cu-2 wt. % rGO i.e. CG has been found to be approximately 130 times lower than that of pure copper (PC). The wear rate shown by the composite Cu-2 wt. % MoS_2, namely, CM is marginally (1.4 times) lower than that of composite CG, whereas the wear rate of the composite Cu- 2 wt. % rGO-MoS_2 i.e. CGM is 6 times less than the wear rate of composite CM as evident from Fig. 6.6.

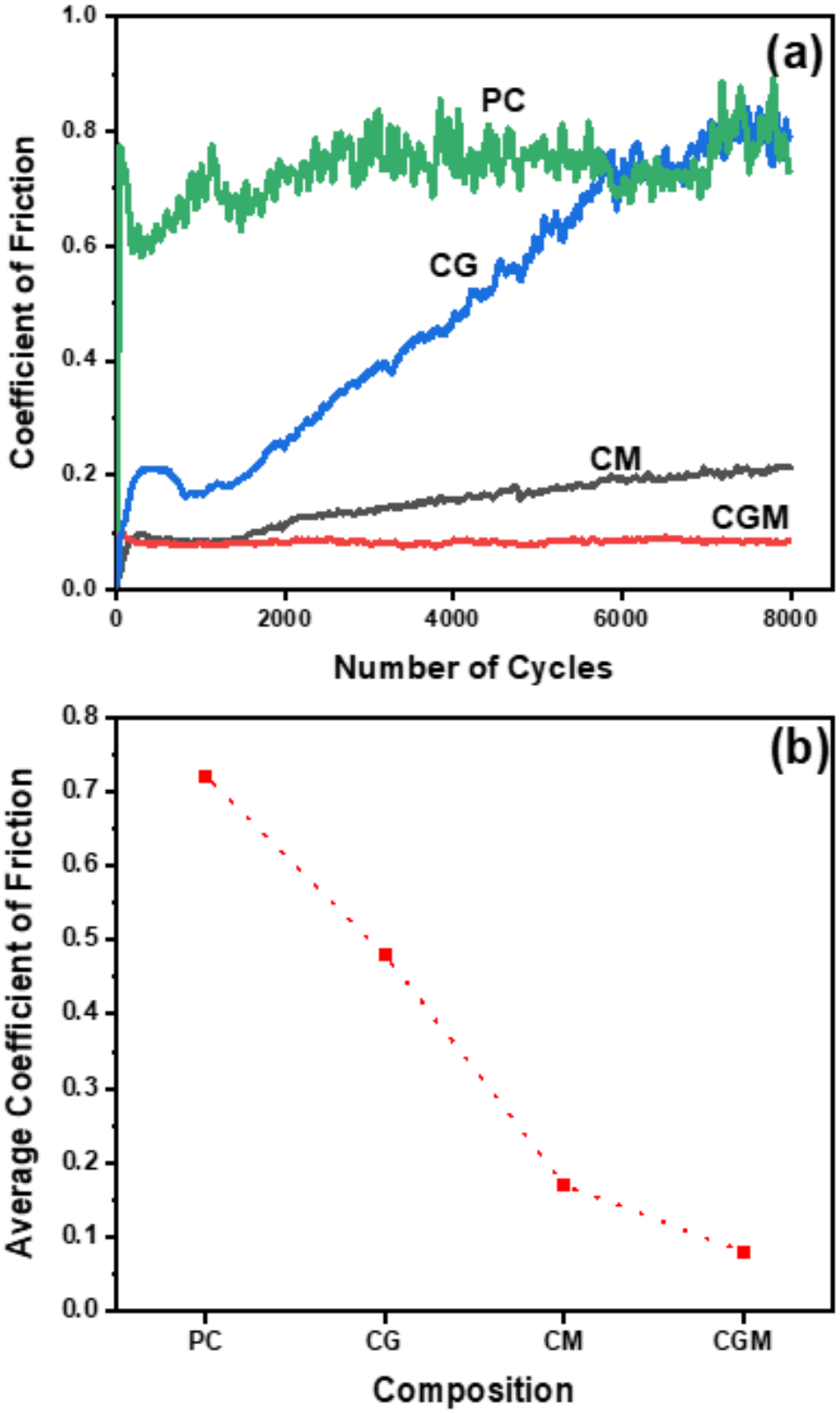

Fig. 6.5 Graphs depicting (a) Real time Coefficient of Friction curve with number of cycles and (b) Variation of average coefficient of friction with Composition. Load: 6N, Sliding speed: 0.5m.s^{-1}.

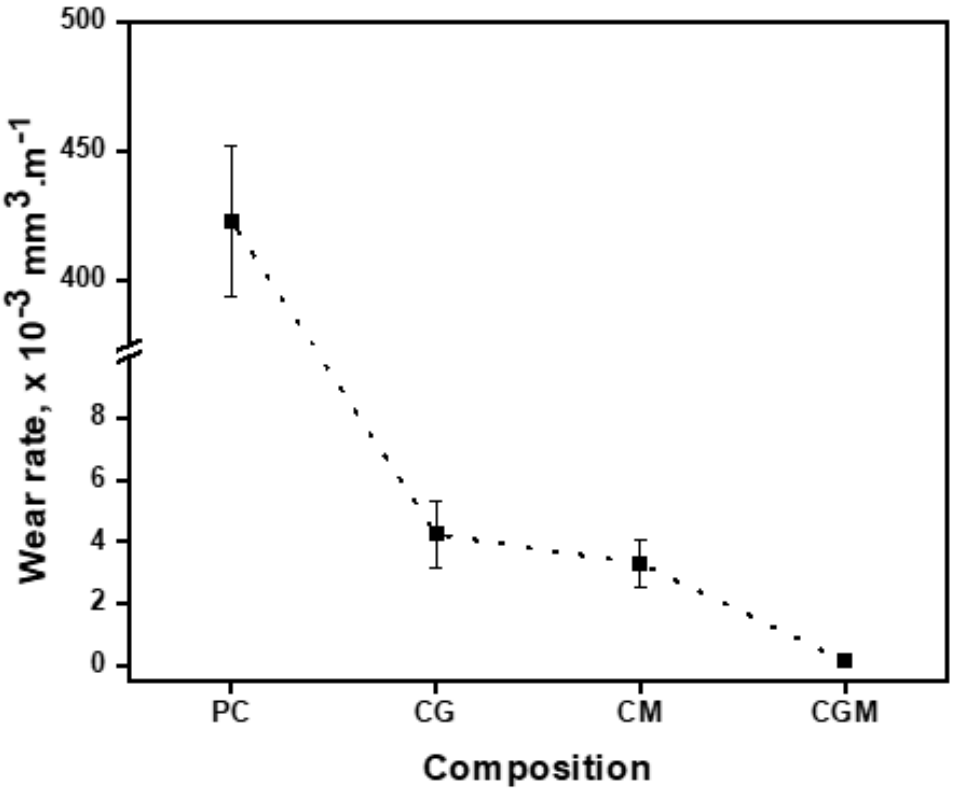

Fig. 6.6 Variation of wear rate with Composition.

The worn surfaces of pure Cu (PC) and composites CG, CM, CGM slid under a load of 6N and 0.5 m. s^{-1} have been examined under the SEM to explore the prevailing mechanisms of wear and the respective micrographs are shown in Fig. 6.7 (a through d). SEM micrograph of the worn surface corresponding to pure copper (PC) shown in Fig. 6.7 (a) reveals a very rough surface and deeply torn surface with signs of adhesion at the edges of wear track and severe abrasion/and ploughing at the middle of the worn track. The worn surface of composite CG given in Fig. 6.7 (b) presents a smooth wear track with no signs of visible sliding marks. However, one may observe the presence of furrows along with a few cracks on the worn track of composite as seen Fig. 6.7 (b), which suggests the occurrence of fatigue assisted wear apart from minor adhesion sites at the edges of the worn track, similar to those seen for pure Cu (Fig. 6.7 a). Figure 6.7 (c) presents the worn track of composite CM, which reveals fine wear marks in the direction of sliding and the presence of a transfer layer at a few places. A relatively smooth wear

track with no signs of abrasion and presence of a smooth tribo-layer over the entire surface along with a very few wear marks in sliding direction could be observed in Fig. 6.7 (d) corresponding to the worn surface of composite CGM.

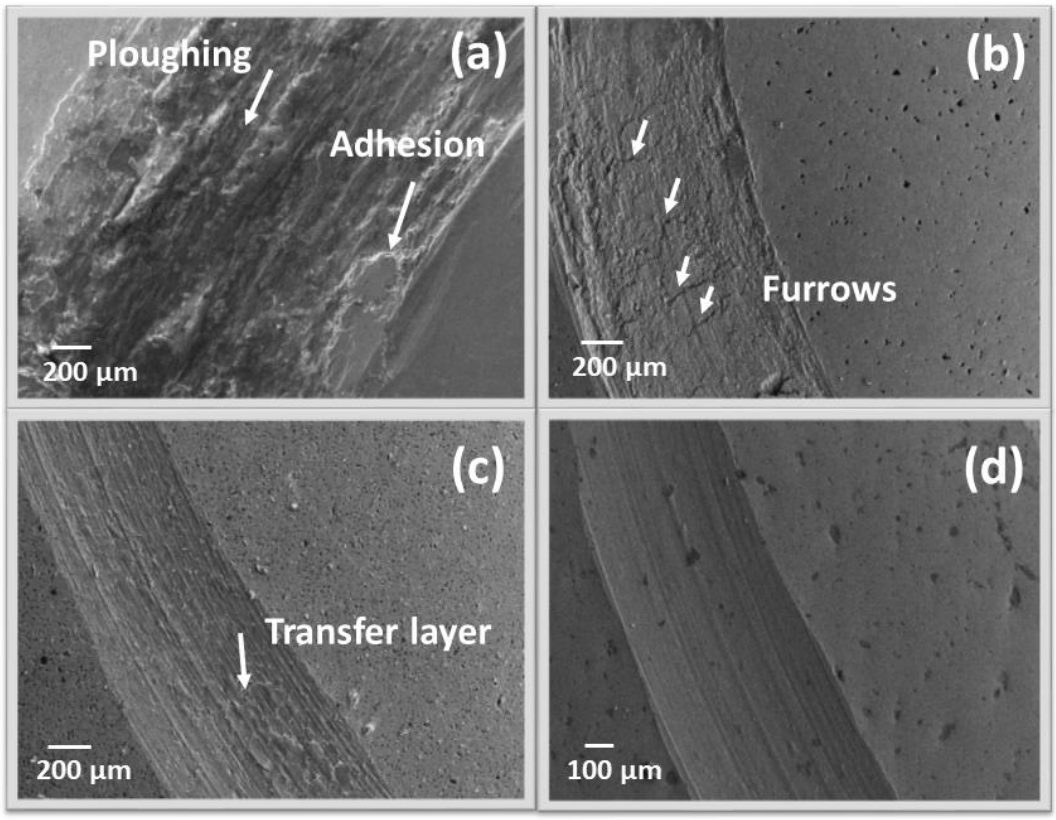

Fig. 6.7 SEM micrographs of the worn surfaces of specimens of (a) PC, (b) CG, (c) CM and (d) CGM, tested at the load of 6 N and 0.5 m. s^{-1}.

Worn track profiles of pure Cu (PC) and composites CG, CM, CGM corresponding to respective SEM micrographs of the worn surfaces depicted in Fig. 6.7, are presented in Fig. 6.8. The worn track of PC presents a relatively uneven track with a width of 2.2 mm and depth of 110 µm, which are the largest whereas the worn track of CGM composite exhibits a very smooth profile curve with a width of 0.6 mm and depth 0.75 µm which are the smallest among all the materials studied in present work as evident from Fig. 6.8. The worn track of CM unveils a width of 0.75 mm and depth of 15 µm with a smooth profile at the bottom of the curve, whereas the worn track of composite CG has

a width of 1.5 mm and depth of 10 µm with a relatively rougher profile in comparison to CM.

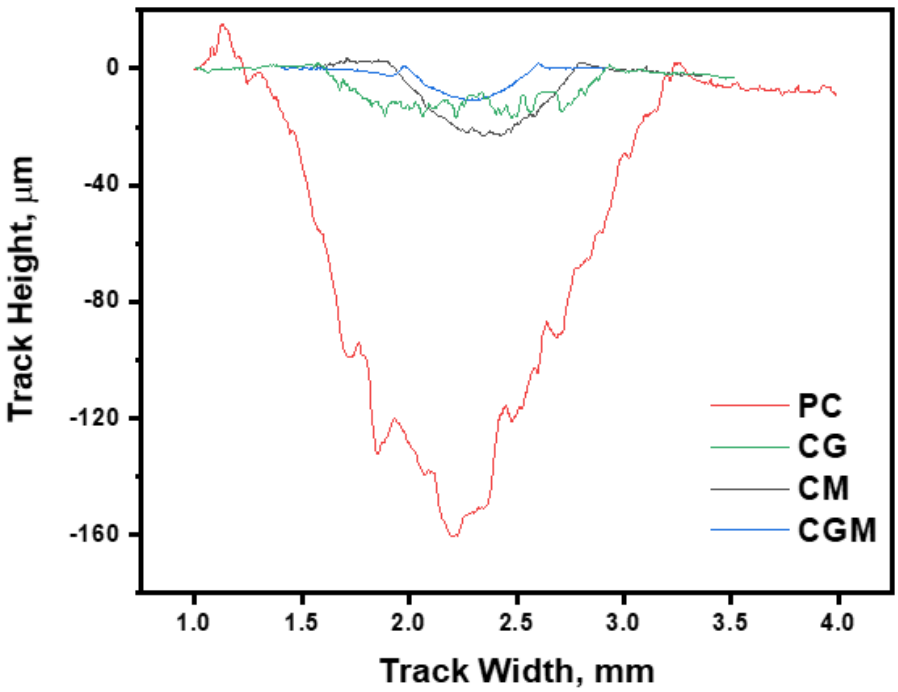

Fig. 6.8 Worn track profiles of (a) PC, (b) CM, (c) CG and (d) CGM.

The worn tracks have been examined to reveal the elemental distribution for eliciting the role of the constituents in affecting the tribological performance under dry sliding conditions. Figure 6.9 (a to c) shows the elemental distribution at the worn tracks of composites CG, CM and CGM, respectively. The elemental distribution on the worn track of CM presented in Fig.6.9 (a) suggests the formation of an oxide layer over the worn surface along with a weak signature of carbon. Figure 6.9 (b) illustrates the elemental distribution of composite CM which also reflects the formation of oxide layer. However, molybedenum and sulfur are found to be absent on the worn track as evident from Fig. 6.9 (b). The elemental distribution of Composite CGM depicted in Fig. 6.9 (c) reveals the formation of transfer layer containing oxides apart from the presence of C, Mo and S on the wear track pointing towards the lubricious nature of the transfer layer.

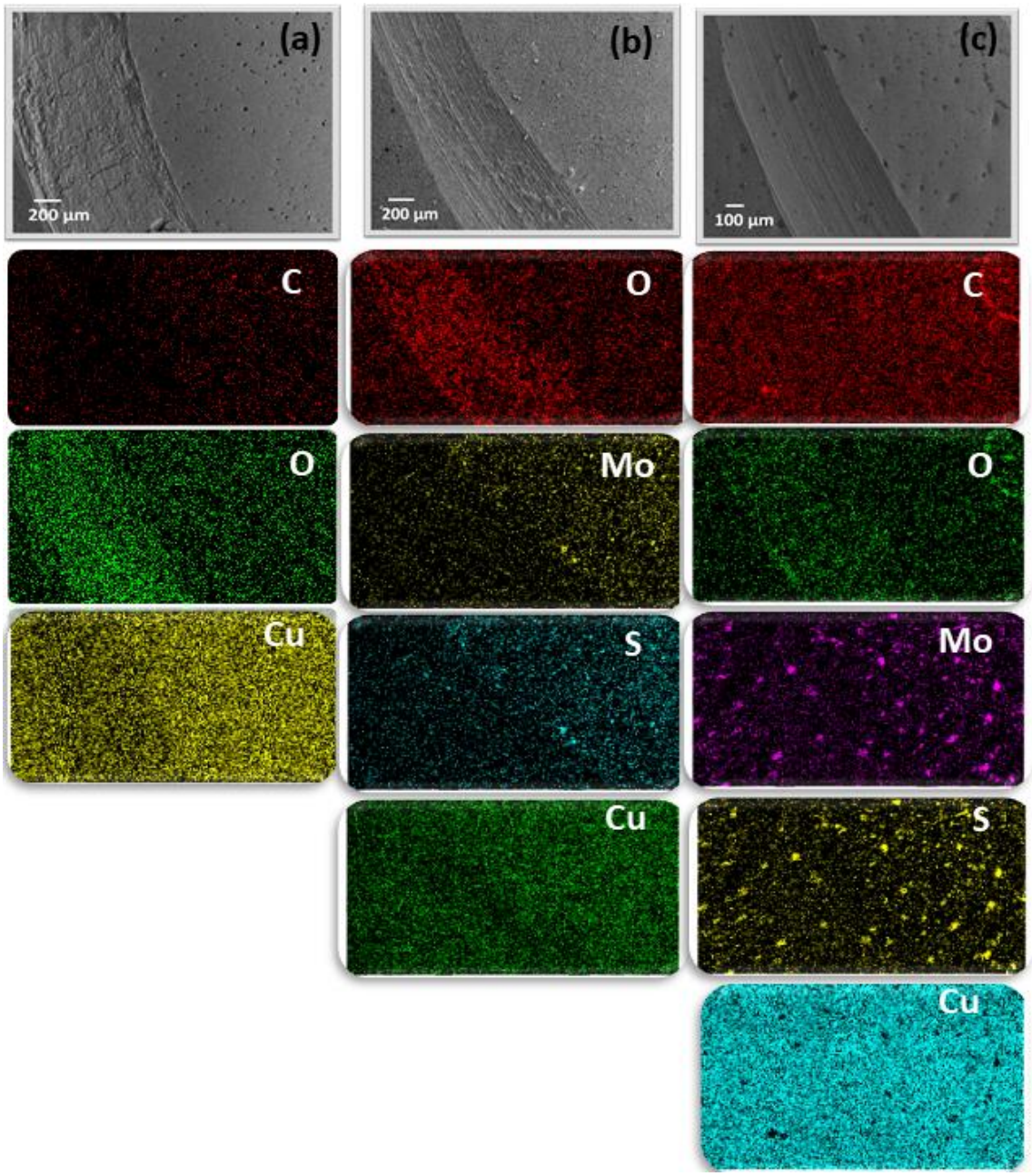

Fig. 6.9 Elemental mapping of worn tracks corresponding to the composites (a) CG, (b) CM and (c) CGM.

In order to get a better insight of the formation of transfer layer in composites CM and CGM, containing either oxides or lubricious species, the worn tracks of these composites have been examined under high magnification and the respective SEM micographs along with their elemental distribution are presented as Figs. 6.10 and 6.11. One may observe the presence of a well developed transfer layer containing oxide and MoS_2 on the worn track of the composite CM given in Fig. 6.10. The elemental distrbution

of worn track of composite CGM shown in Fig. 6.11 reveals the presence of C, Mo and S which appear to be distributed over the entire worn surface, suggesting thus the formation of a thin tribo-layer rich in graphene and MoS_2 and an oxide layer.

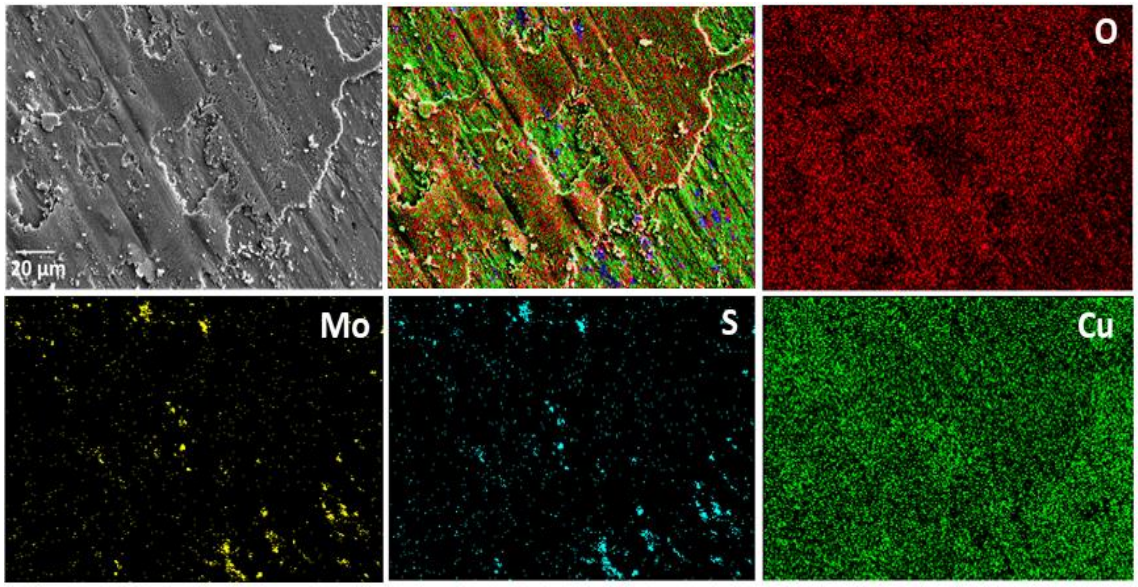

Fig. 6.10 Elemental mapping of worn surface corresponding to CM composite depicting the formation of oxide layer.

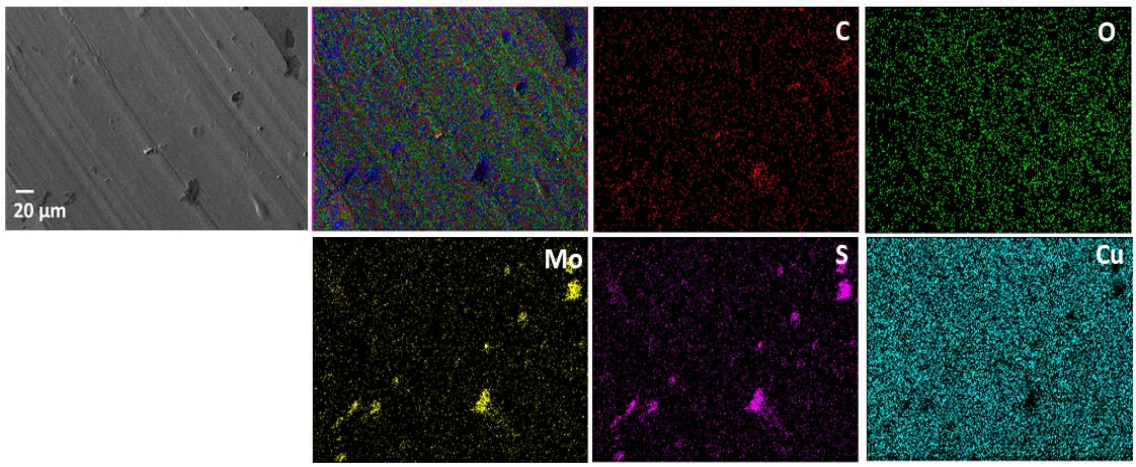

Fig. 6.11 Elemental mapping depicting tribo-layer formation over the worn surface of CGM composite.

Figure 6.12 (a through d) shows the worn surface micrographs of EN31 balls used as the counterface to slid against pure copper and composites. The worn scar corresponding to specimen PC shown in Fig. 6.12 (a) presents the abrasive features

covering a larger portion of the micrograph. One may observe minor abrasion on the worn surface of steel ball slid against composite CG with relatively smaller worn scar as compared to that of specimen PC along with some adhesion at the edge of worn scar as evident from Fig. 6.12 (b). However, the worn scar on the counter face slid against composite CM presented in Fig. 6.12 (c) shows a relatively smooth surface with few minor abrasion marks. The micrograph of the worn surface of the steel ball slid against composite CGM reveals the presence of a transfer layer as seen in Fig. 6.12 (d). The area of worn scar on the ball slid against CGM also appears to be the smallest among all which may be judged from a comparison of Figs. 6.12 (a through d).

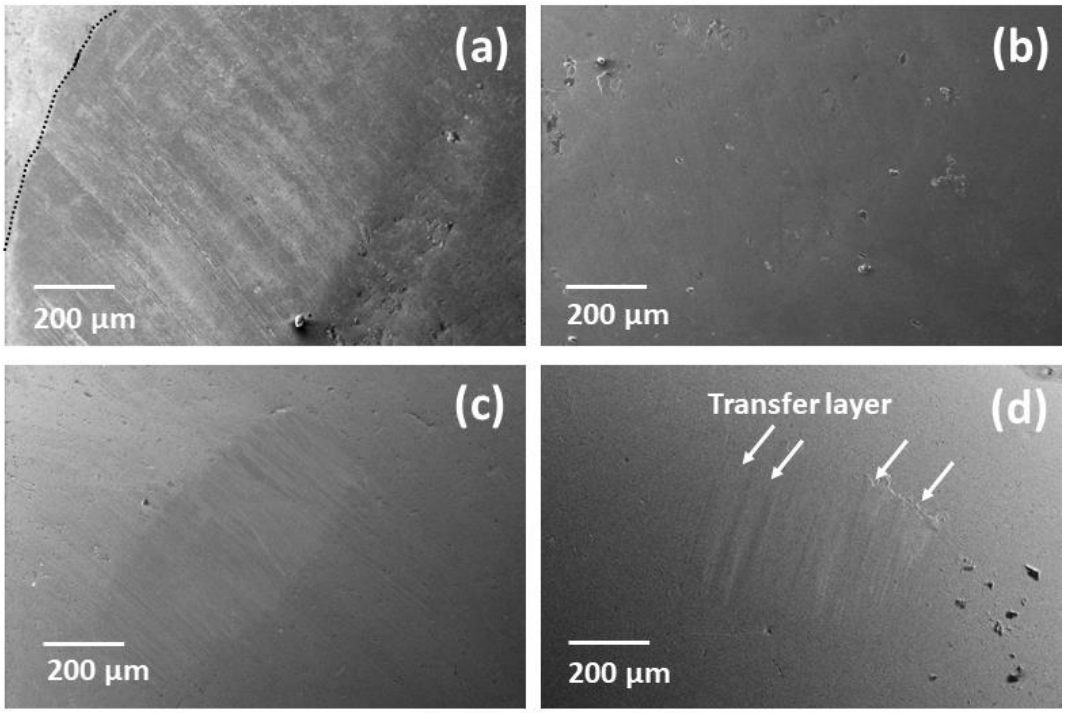

Fig. 6.12 SEM micrographs of the worn surfaces of counter ball slid against (a) PC, (b) CG, (c) CM and (d) CGM

The presence of transfer-layer on the counter face corresponding to composite CGM observed in Fig. 6.12 (d) is confirmed by the elemental mapping of the worn scar presented in Fig. 6.13, which reveals the formation of a well-developed transfer layer in the form of stripes as indicated by elemental distribution and the presence of graphene,

MoS_2, copper and lubricious oxide phase containing Cu, C, Mo, S as suggested the by elemental overlay.

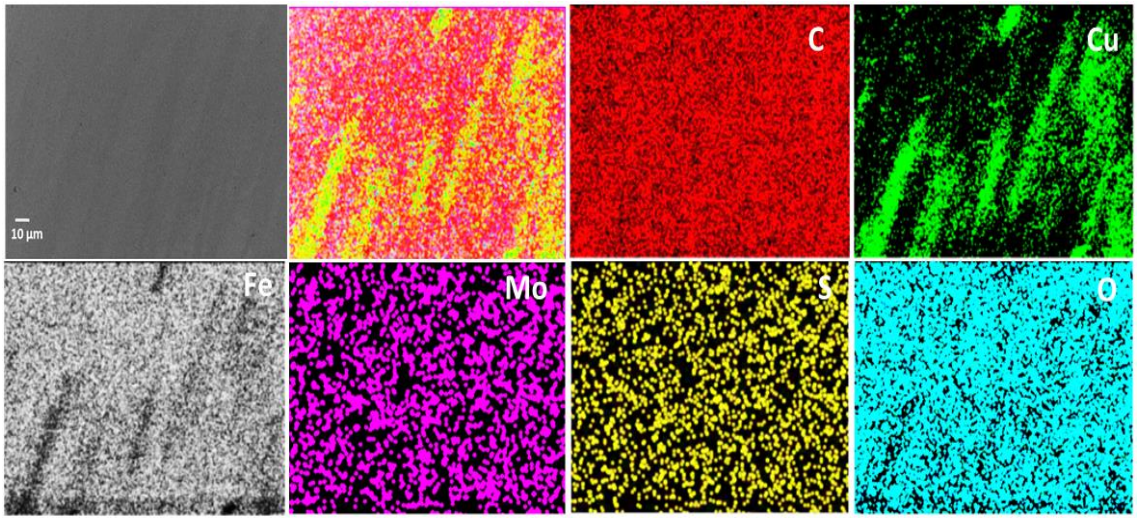

Fig. 6.13 Elemental mapping of counter face corresponding to composite CGM depicting the formation of transfer layer over the surface.

The subsurface region micrographs analysis is useful for unveiling the various features pertaining to tribo-testing like plastic deformation, tribo-layer formation, etc. Figure 6.13 shows the micrograph corresponding to PC, CG, CM and CGM composite subsurface region, which have been tested at the load of 6N and 0.5 $m.s^{-1}$ sliding speed against EN31 ball. Micrograph of PC specimen's subsurface region is shown in Fig. 6.13 (a), low magnification micrograph is shown with its corresponding high magnification micrograph shown in the inset depicts the severe plastic deformation. Whereas, facets with cracks can be clearly observed in the case of subsurface micrograph corresponding to composite CG shown in Fig. 6.13 (b), which is the characteristics of brittle failure. Figure 6.13 (c) shows the micrograph of subsurface region corresponding to CM composite, a discontinuous layer formation can be observed, which is inclusive of 2-3 µm thick fragments. A very thin film of 1-1.5 µm can be seen over the subsurface region corresponding to composite CGM, indicated by arrows as shown in Fig. 6.13 (d).

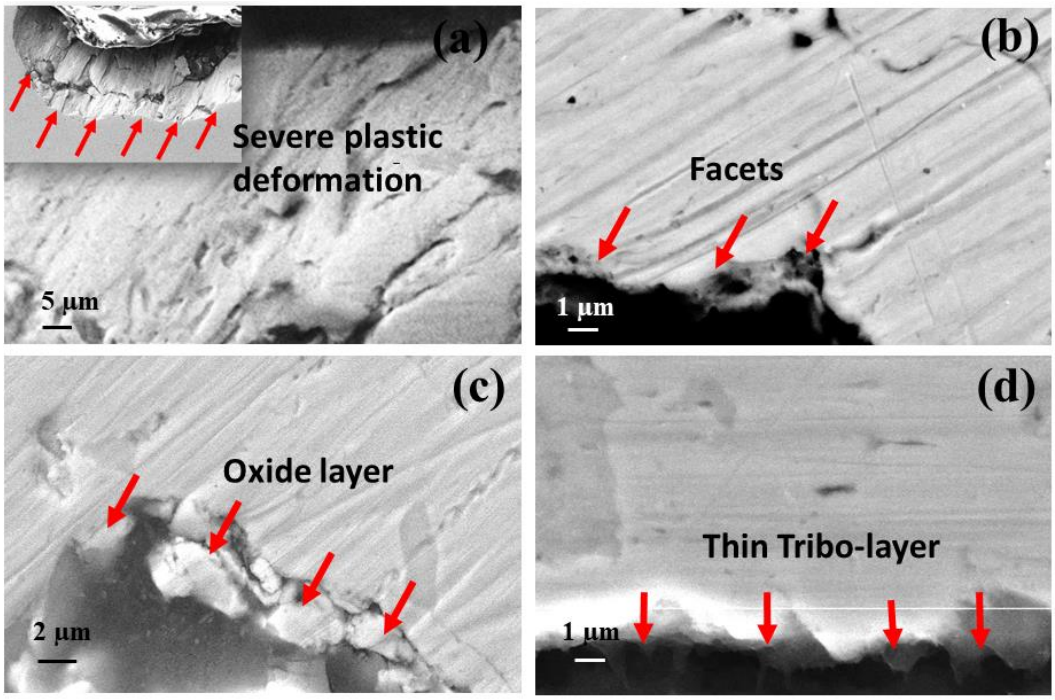

Fig. 6.14 SEM micrographs of subsurface region for the sample (a) PC, (b) CG, (c) CM and (d) CGM. Inset of the Fig. 6.14 (a) shows the high magnification micrograph for sample PC subsurface region.

Raman spectra of two separate points corresponding to the worn and unworn regions of composite CGM given in Fig. 6.15 the clearly reveals the D and G bands of graphene. One may also observe the presence of E^1_{2g} and A_{1g} bands corresponding to MoS_2 shown in expanded region of spectrum marked by ellipse given in the inset. Both E band and A band peaks could be seen for worn as well as unworn area at the 367 and 411 cm^{-1}, respectively. The existence of a broad peak at 810 cm^{-1} indicates the presence of MoO_3 phase, for both worn and unworn regions as evident from Fig. 6.15. However, a relatively high intensity of MoO_3 peak at the worn track suggests the occurrence of tribo-oxidation. The intensity ratio (I_D:I_G) for graphene is observed to be more for unworn surface (I_D:I_G = 1.2) than that for the worn track (I_D:I_G = 0.96) as seen from Fig. 6.15.

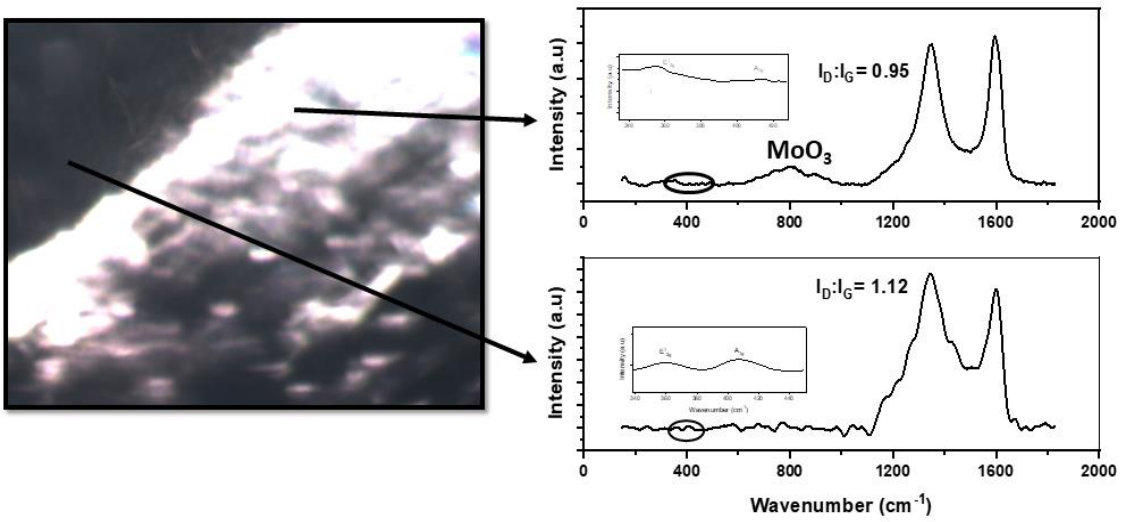

Fig. 6.15 Raman spectra of two separate points taken from unworn and worn surface of composite CGM.

6.2 DISCUSSION

The characteristic diffraction features of composites PC, CG, CM, CGM shown in Fig. 6.3 reveal sharp peaks at 2θ of 43.3 and 50.4° corresponding to (111) and (200) planes of pure copper in all the composites. The presence of comparatively weak peak at 26.5° corresponding to (002) plane of rGO can be seen for the diffraction pattern of CG composite, weak signature of rGO peak accounts for low content (< 5 wt.%) of material, while similar type of weak signature of MoS_2 can be observed at the 33.4° for the composite CM. Diffraction pattern corresponding to CGM composite shown in expanded inset reveal three peaks for three distinct phases at 2θ of 26.5°, 33.4° and 36.4°, respectively, for (002) plane of rGO, (101) plane of MoS_2 and (111) plane of MoC. The emergence of MoC phase peak at 36.4° is believed to be the result of chemical interaction between MoS_2 and GO during ball milling and high temperature and pressure environment during SPS.

The hardness and density of pure Copper and composites given in Table 6.1 indicate an increase in hardness with addition of reinforcements in pure copper whereas a decrease in density is observed with the second phase addition. Pure copper exhibits the maximum density of 8.62 $g.cm^{-3}$, which is followed by specimen CGM having the density of 7.48 $g.cm^{-3}$, density of CM is found to be minimum, i.e. 6.95 $g.cm^{-3}$ which may be ascribed to the voids formation, as observed in Fig. 6.1 (c). A relatively lower hardness observed for pure copper despite having high density may be attributed to the inherent softness and ductile nature of copper, while the high hardness of composites compared to that of pure copper could be ascribed to the Orowan strengthening mechanism (Ghambhari et al. 2020). However, as far as composites are concerned, the density and hardness are observed to be in consonance i.e. the denser the composite the higher is the hardness, which is confirmed by a critical analysis of the microstructure of the composites illustrated in Figs. 6.1 (b, c and d). The presence of voids observed in the microstructure of composite CM (Fig. 6.1 c) leads to a reduction in density with a consequent reduction in hardness, whereas less number of voids visible in the micrograph of CG (Fig. 6.1 b) may explain it's relatively high hardness in comparison to CM. The highest hardness shown by CGM may be attributed to its dense and void free microstructure assisted by the uniform distribution of second phase as evident from Fig. 6.1 (d). Moreover, hard phase MoC formation demonstrated by XRD in Fig. 6.3, might have also contributed to the increase in hardness for CGM composite.

The variation of coefficient of friction with number of cycles for PC and composites is shown in Fig.6.5 (a) tested at a load of 6N and 0.5 $m.s^{-1}$ sliding speed against EN31 steel ball. A fluctuating trend can be observed for the composites and pure copper, fluctuation of friction coefficient could be attributed to variation in contact between surface and counter surface, while trying to attain a better conformity. However,

the fluctuations as well as average coefficient of friction and the wear rate are observed to decrease as one moves from pure Copper to CG to CM to CGM as evident from Figs. 6. 5 (a and b) and Fig.6.6. The observed decrease in coefficient of friction and wear rate with changing composition may be explained on the basis of (i) the SEM micrographs of the worn surfaces of PC, CG, CM and CGM and the counterface balls slid against these, (ii) the elemental mapping of their worn tracks and (iii) presence of distinct features on the subsurface of the worn specimens.

The high coefficient of friction (Fig. 6.5 b) and wear rate (Fig. 6.6) shown by pure Copper may be attributed to the plastic deformation and presence of deeper grooves along with signs of adhesion on the worn surface as evident from Fig. 6.7 (a) and abrasive marks on the worn surface of the ball slid against PC as seen from 6.12 (a) which might have led to the occurrence of direct metal-metal contact between the mating bodies and consequently in high friction and high loss or material. The largest height and depth of the worn tack for PC as shown in Fig. 6.8 also confirms a higher loss of material and hence, a higher wear rate. A relatively larger size wear scar on the worn surface of ball slid against pure copper as seen from Fig. 6.12 (a) also indicates a larger loss of material due to wear. The subsurface micrograph for pure copper shown in Fig. 6.14 (a) reveals the severe plastic deformation below the sliding surface which may explain a relatively higher wear rate in PC. The other contributing factor may be the relatively lower hardness of pure copper (Table. 6.1), because of which it is not able to resist the deformation under the applied load.

A significant reduction in coefficient of friction and wear rate shown by composite CG in comparison to PC may be explained on the basis of the morphologies of the worn surface of CG presented in Fig 6.6 (b) which shows the presence of furrows, against the deeper groves shown by PC (Fig. 6.6 a) and the worn surface of the ball slid

against CG which shows a relatively smooth surface (Fig. 6.12 b) as compared to the ball slid against PC which reveal some abrasive marks (Fig. 6.12 a). The worn tack profiles given in Fig. 6.10 also confirm a significantly lower wear rate in CG as compared to PC**.** A reduced coefficient of friction and wear rate in composite containing graphene may be attributed to the presence of graphene which provides self-lubricating characteristics due to its inherent lubricious nature. However, the elemental mapping of the worn surface of CG given in Fig. 6.9 (a) suggest that worn track is lean in carbon content indicating that lubricious nature of graphene is not the sole factor responsible for reduced friction and wear rate. The other contributing factor may be the presence of oxide layer as revealed by elemental mapping (Fig. 6.9 a) probably comprising Cu_2O, assuming that there is zero possibility of any other type of oxide formation. The oxide layer provides low shearing strength junctions and also inhibits direct metal-metal contact between the mating bodies (Zhang et al., 2019) The presence of relatively lower content of carbon on the worn track may be attributed to the loss of graphene sheet that may occur during sliding due to the poor interfacial bonding of graphene with copper which act as crack initiation sites and eventually lead to fatigue wear as suggested by furrows seen in Fig. 6.7 (b). The poor interfacial bonding at copper and graphene interface can be judged from the micrograph of CG composite shown in Fig. 6.1 (b), where one may observe the agglomeration of GO. The micrograph of the subsurface of composite CG given in Fig. 6.14 (b) hardly shows any sign of plastic deformation rather facets indicative of brittle failure of material could be clearly seen which further confirms the fatigue failure suggested by the presence of furrows on the worn surface micrograph of CG given Fig. 6.7 (b).

The composite CM containing MoS_2 exhibits a lower coefficient of friction and wear rate than CG containing rGO and the observed decrease may be explained with the help of worn surface of CM, its elemental distribution and the worn surface of ball

slid against CG presented, respectively, as Fig. 6.7 (c), 6.9 (b) and 6.12 (b). The worn track shown in Fig. 6.7 (c) indicates the minor abrasive wear along with the presence of a tribo-layer consisting of oxide and MoS_2, the presence of which has been confirmed by the elemental mapping shown in Figs. 6.9 (b) and 6.10, respectively. The SEM micrograph of the subsurface of the composite CM illustrated in Fig. 6.14 (c) has also revealed the presence of a fragmented tribo-oxide layer. The formation of tribo-layer brings about a reduction in coefficient of friction and wear rate by restricting the metal-metal contact while simultaneously providing the easy to shear interface between the mating surfaces as explained earlier. A relatively smooth worn surface of the ball slid against CM shown in Fig. 6.12 (c) indicates the occurrence of smooth sliding between ball and CM due to the absence of any adhesion or material transfer reflecting a relatively lower material loss in comparison to that for ball-CG tribo-pair. Also, the tribo-layer appears to have covered a larger area of the worn surface corresponding to CM (Fig. 6.7 c) as compared CG (Fig. 6.7 b) through which it is able to provide a better protection to the underlying substrate against both friction and wear. This may explain a relatively lower coefficient of friction and wear rate in CM in comparison to CG, despite the formation of a tribo layer on CG.

The composite CGM containing rGO-MoS_2 hybrid has shown the lowest coefficient of friction and wear rate among all the composites as evident from Figs. 6.5 and 6.6, The observed behavior may again be explained on the basis of the worn surface micrographs of CGM and counterface ball along with the elemental mapping shown in Figs.6.7 (d), 6.12 (d) and 6.9 (c). The worn surface of CGM (Fig. 6.7 d) presents a smooth track with no signs of abrasion or adhesion as compared to PC (Fig. 6.7 a), CG (Fig. 6.7 b) and CM (Fig. 6.7 d), also confirmed by the profilometry of the worn tracks shown in Fig. 6.10 which demonstrate a smooth profile with less width and depth for CGM as

compared to other composites and pure copper, indicating a low wear rate and coefficient of friction. In order to further reveal the factors responsible for the observed behavior of CGM, elemental mapping of the worn surface is conducted which reveals the presence of O, Mo, S and C on the worn surface as evident from Fig. 6.9 (c) and the presence of a smooth tribo-layer over the worn track comprising probably of oxides, graphene and MoS_2 as evident from Fig.6.11. The presence of MoO_3 which is lubricious in nature has been confirmed by the Raman analysis given in Fig. 6.15. The formation of a tribo-layer formation is further confirmed by the subsurface analysis, which depicts a dark grey shaded thin film of 1 µm thickness, indicated with the help of arrows in the Fig 6.14 (d). Also, worn surface of the counterface ball slid against CGM exhibits the smallest worn scar and indicates the transfer of the material as seen in Fig. 6.12 (d). The transfer of the material from the CGM composite is confirmed by the elemental mapping presented in Fig. 6.13, which demonstrates the presence of Cu, C, Mo, S and oxygen on the worn surface of the ball. The existence of a tribo-layer on the worn surface of CGM and the transfer of material containing solid lubricants to the ball surface results in the avoidance of direct metal-metal contact between the ball and composite while simultaneously providing a low shearing interface due to presence of lubricating species leading a low coefficient of friction and low wear rate. Hence, the lowest coefficient of friction and wear rate is observed for CGM in comparison to other composites and pure Copper.

The presence of salient features on the worn surfaces of pure Copper and composites indicate that the wear mechanism is a combination of abrasion and adhesion for PC, whereas the same for rGO reinforced composite i.e. CG is a combination of fatigue, abrasion and adhesion. However, the wear mechanism for MoS_2 reinforced composite (CM) is a mixture of minor abrasion and oxidation, whereas it is mild oxidation for Cu-rGO-MoS_2 (CGM) composite.

The present investigation has been carried out to explore the effect of the addition rGO, MoS_2 and rGO-MoS_2 hybrid nano particles on the mechanical and tribological behavior of Cu based composites prepared by spark plasma sintering and to examine the possibility of a synergistic action between rGO and MoS_2 in improving the tribological performance of such composites. The hardness of the pure Copper has been found to increase with addition of the reinforcements. However, among the composites Cu-rGO-MoS_2 composite has shown the highest hardness, which has attributed to the good interfacial interaction bonding between rGO-MoS_2 and copper. The composites have shown a significantly lower coefficient of friction and wear rate in comparison to pure Copper. Among the composites, Cu-2 wt. % rGO-MoS_2 (CGM) has demonstrated the lowest coefficient of friction (~0.08) and wear rate, whereas Cu-2 wt. % rGO (CG) has shown the highest. The coefficient of friction and wear rate shown by the composite Cu-2 wt. % MoS_2 (CM) falls in-between. The lowest coefficient of friction and wear rate shown by CGM have been attributed to the presence of a tribo-layer consisting of graphene, MoS_2 and MoO_3 on the worn surface and the transfer of material from composite to counterface ball which provides low shearing properties at the interface and protects the underlying substrate from direct metal-metal contact. A relatively higher coefficient of friction and wear rate shown by CG have been attributed to the abrasion, adhesion and fatigue and absence of any tangible tribo-layer on the worn surface. However, a moderate friction coefficient and wear rate shown by MoS_2 reinforced composite have been attributed to the combination of abrasion and tribo-oxidation. The results indicate the occurrence of a synergistic action of rGO-MoS_2 in reducing the coefficient of friction as well as wear rate. Hence, further study has been conducted to examine the effect of rGO-MoS_2 content on the tribological performance of Cu-rGO-MoS_2 composites by carrying out friction and wear tests at different loads and a constant

sliding speed to determine the optimum content of addition and the results are presented in section 6.3.

6.3 TRIBOLOGICAL BEHAVIOR OF COMPOSITES CONTAINING (0.5, 1.0, 1.5 and 2.0 wt. % rGO-MoS_2 hybrid) AND AT DIFFERENT LOADS

The friction and wear characteristics of Cu-rGO-MoS_2 nanocomposites have been evaluated under dry sliding conditions against the steel ball at different loads of 4, 6, 8, and 10 N and constant speed of 0.5 m. s^{-1}. Figure 6. 16 (a to d) shows the variation of coefficient of friction with number of cycles at different loads for all the composites, namely, CGM 0.5, CGM 1.0, CGM 1.5 and CGM 2.0 containing, respectively, 0.5, 1.0, 1.5 and 2.0 wt. % rGO-MoS_2. All the composites have been found to show a fluctuating trend of variation with varying amplitudes of fluctuations. However, the amplitude of fluctuations has been observed to decrease with increasing content of rGO-MoS_2 which is evident from a comparison of the curves given in Fig. 6.16 (a through d) where CGM 0.5 has the largest amplitude of fluctuation whereas CGM 2.0 has the smallest at all the loads as evident from a comparison of Figs. 6.16 (a through d). Also, the composite CGM 2.0 has shown a relatively stable nature of variation at all the loads. At a particular load (say 10 N), composite CGM 0.5 has been observed to exhibit the highest coefficient of friction (μ ~1.0) throughout the tribo-test, which is followed by the composite CGM 1.0 (containing 1 wt. % of rGO-MoS_2) which has shown a little lower coefficient of friction (μ ~ 0.8), than composite CGM 0.5. One may observe that the coefficient of friction for composite CGM 1.5 is significantly lower (μ ~ 0.2) for initial 950 sliding cycles, which increases abruptly beyond that and reaches a value of 0.7 but, with reduced amplitude of fluctuations as from Fig. 6.16 (a). The CGM2.0 nanocomposite having 2.0 wt. % of rGO-MoS_2 nanofiller has been found to show a significantly low and stable coefficient of

friction ($\mu \sim 0.2$) with negligible fluctuations over the entire duration of the test. A similar behavior could be observed at other loads of 4, 6 and 8 N with varying number of cycles during which a particular composite has shown a low coefficient of friction before reaching a high and stable value during the test.

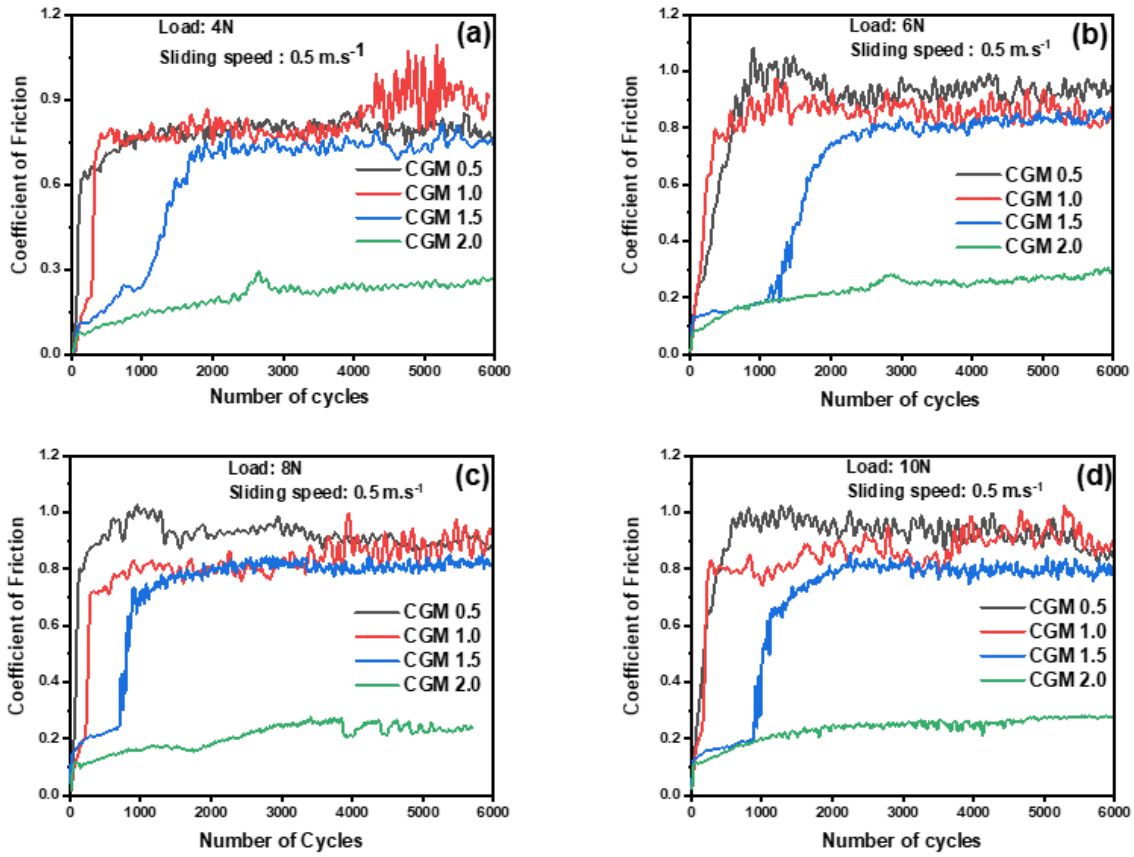

Fig. 6.16 Variation of Coefficient of friction with number of cycles against the steel ball under the load of (a) 4 N, (b) 6N, (c) 8N and (d) 10N.

Figure 6.17 (a) depicts the variation of the average coefficient of friction with load for all the composites, namely, CGM0.5, CGM1.0, CGM1.5 and CGM2.0. The average coefficient of friction for each test has been estimated after the stabilization of friction curve in the variation of coefficient of with number of cycles. A marginal increase in the average coefficient of friction with increasing load could be observed for all the composites in Fig. 6.17 (a) except CGM 0.5 which shows a slight decrease with an increase in load from 4 to 8 N followed by an increase beyond that. The variation of

average coefficient of friction with composition shown in Fig. 6.17 (b) reveals that the average coefficient of friction decreases with an increasing amount of rGO-MoS_2. One may observe that a marginal change in the average coefficient of friction as the content of rGO-MoS_2 is raised from 0.5 to 1.5 wt. % at all the loads. However, a sharp reduction in average coefficient of friction could be observed as the content of rGO-MoS_2 is increased from 1.5 to 2.0 wt. % as evident from Fig. 6.17 (b). It may also be observed that the composite containing 2.0 wt. % rGO-MoS_2 i.e. CGM2.0 has the lowest coefficient of friction at all the loads used in the present study.

Figure 6.18 (a) and (b) illustrate the variation of wear rate with load and the composition, respectively. The wear rate has been observed to increase with increasing load from 4 to 10 N as evident from Fig.6.18 (a). However, the increase is marginal for the composites CGM0.5 and CGM2.0 whereas a relatively higher increase in wear rate with load could be seen for CGM1.0 and CGM1.5. One may also observe that the increase in wear rate for CGM1.0 is relatively sharper in comparison to CGM1.5 as the load is raised from 4 to 8 N. However, beyond 8 N both the composites (CGM1.0 and CGM1.5) appears to have the same rate of increase as evident from an almost parallel line in Fig. 6.18 (a) as the load in increased from 8 to 10 N. The composite CGM 0.5 has shown the minimum wear among all composites whereas CGM 1.0 has shown the maximum wear rate at all the loads as evident from Fig. 6.18 (b). An increase in rGO-MoS_2 content beyond 1.0 wt. % results in a decrease in wear rate as seen in Fig. 6.18 (b). One may observe that the decrease is sharp at relatively higher loads as seen from Fig. 6.18 (b) which indicates a relatively sharp decrease with increasing load from 4 to 8 N. The wear rate of CGM 2.0 nanocomposite having a 2 wt. % of rGO-MoS_2 filler is found to be significantly low and close to that of CGM 0.5 composite as seen from Fig. 6.18 (b).

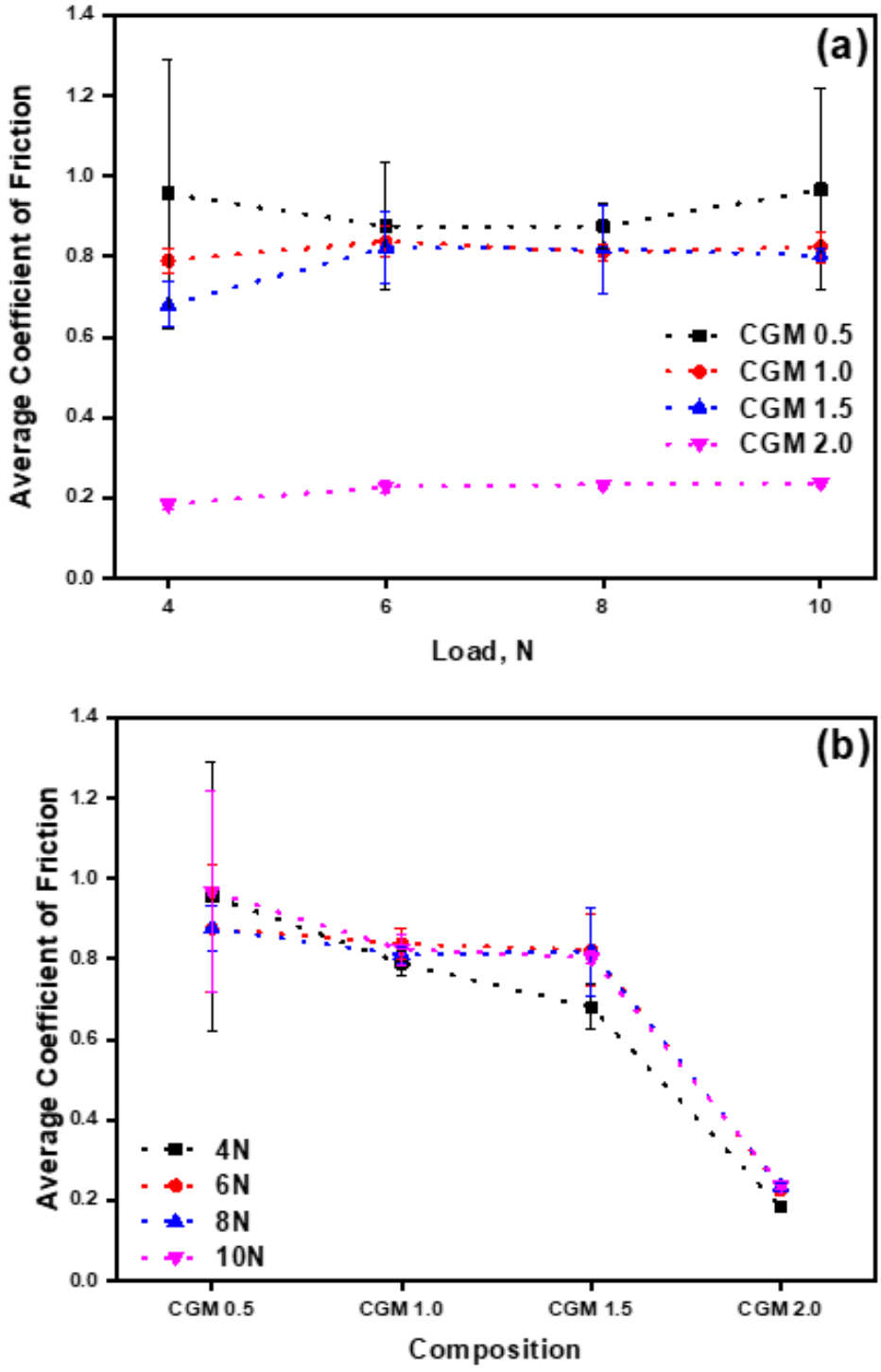

Fig. 6.17 (a) Variation of average coefficient of friction with applied load and (c) Variation of average coefficient of friction with composition.

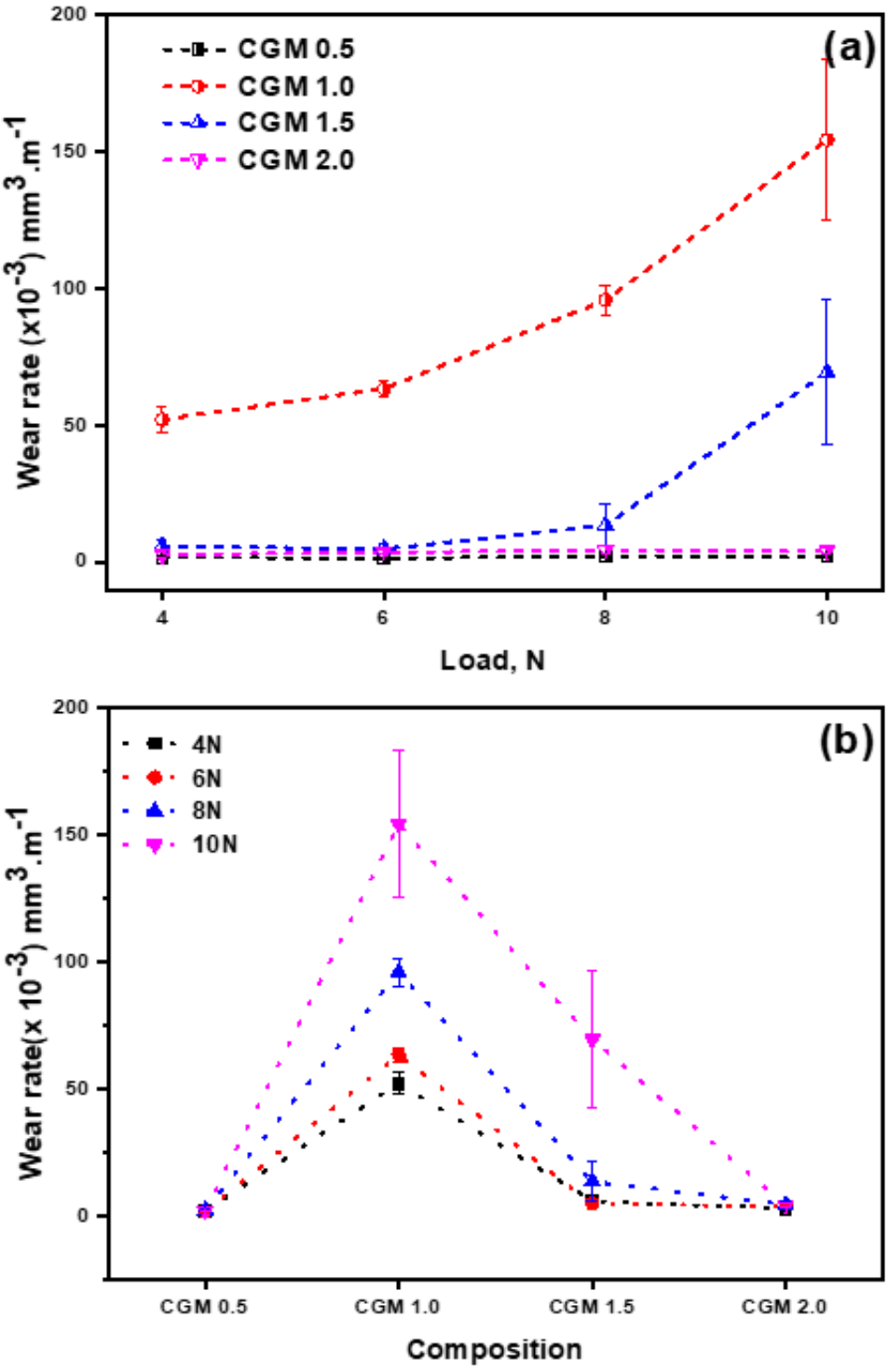

Fig. 6.18 (a) Variation of wear rate with load for composites and (b) Variation of wear rate with composition at different loads.

Figure 6.19 shows the scanning electron micrographs of worn surfaces of Cu-rGO-MoS_2 nanocomposites slid against steel ball under a load of 4 N. The worn track of CGM 0.5 nanocomposite (Figure 6.19 a) suggests adhesion and oxidation-driven wear

events as the major wear mechanism. The micrograph of the worn surface of CGM 1.0 nanocomposite (Figure 6.19 b) indicates a severe abrasion-driven wear mechanism along with the delamination of the material. The severe abrasive marks on the worn surface suggest the abrasions by worn particles. The presence of worn particles at tribo-interface indicates the peeling-off of the tribo-layer from the micrograph corresponds to the worn area of CGM 1.5 (Figure 6.19 c). The worn surface micrograph of CGM 2.0 composite (Figure 6.19 d) containing 2 wt. % rGO-MoS_2 shows the formation of the compact layer with minor abrasion sites.

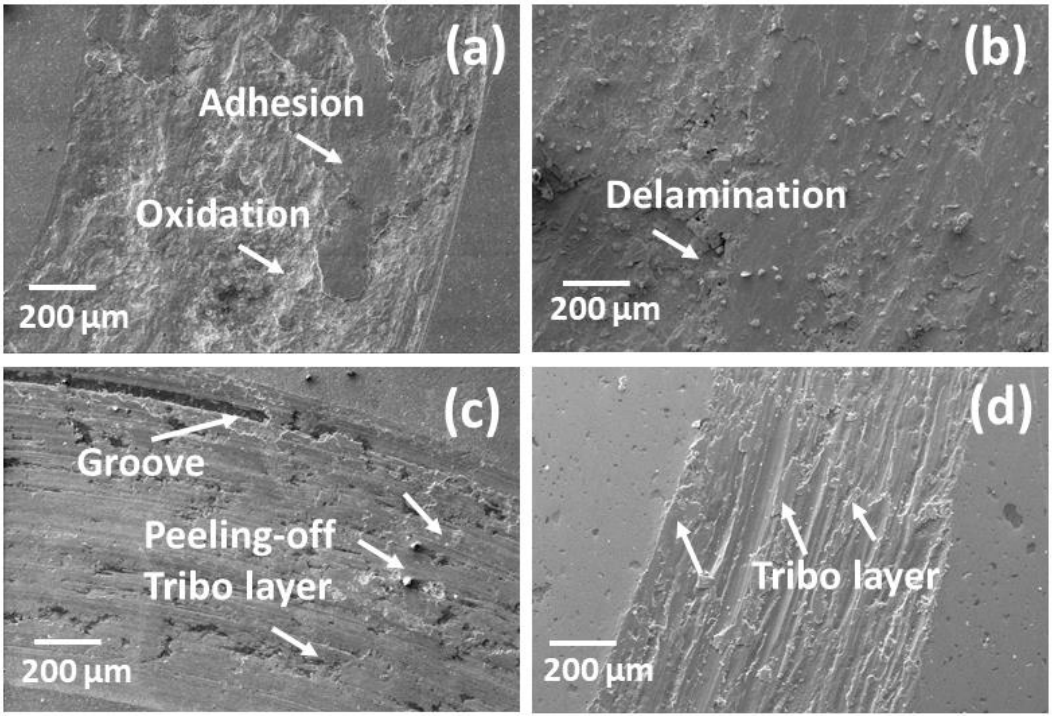

Fig. 6.19 Worn surface micrograph of composites (a) CGM 0.5, (b) CGM 1.0, (c) CGM 1.5 and (d) CGM 2.0, tested at the load of 4N and sliding speed 0.5 $m.s^{-1}$.

Fig. 6.20 shows the micrographs of worn surfaces of Cu-rGO-MoS_2 nanocomposites after the tribo-tests against steel ball under the load of 10 N. The worn track of CGM0.5 nanocomposite (Fig. 6.20 a) suggests adhesion and oxidation-driven wear events as the major wear mechanism. The micrograph of the worn surface of CGM1.0 nanocomposite (Fig. 6.20b) indicates a severe abrasion-driven wear mechanism

along with the delamination of the material. The severe abrasive marks on the worn surface indicate the abrasion caused by worn particles. The worn surface of CGM1.5 given in Fig. 6.20(c) shows the presence of worn particles spread all over the worn area along with the presence of a the tribo-layer which appears to have been peeled off by the worn particles present at tribo-interfaces. The worn surface micrograph of CGM2.0 nanocomposite containing 2 wt. % rGO-MoS_2 nanofiller indicates the presence of a compacted layer of wear debris containing probably the rGO-MoS_2 phase as evident from Fig. 6.20 (d).

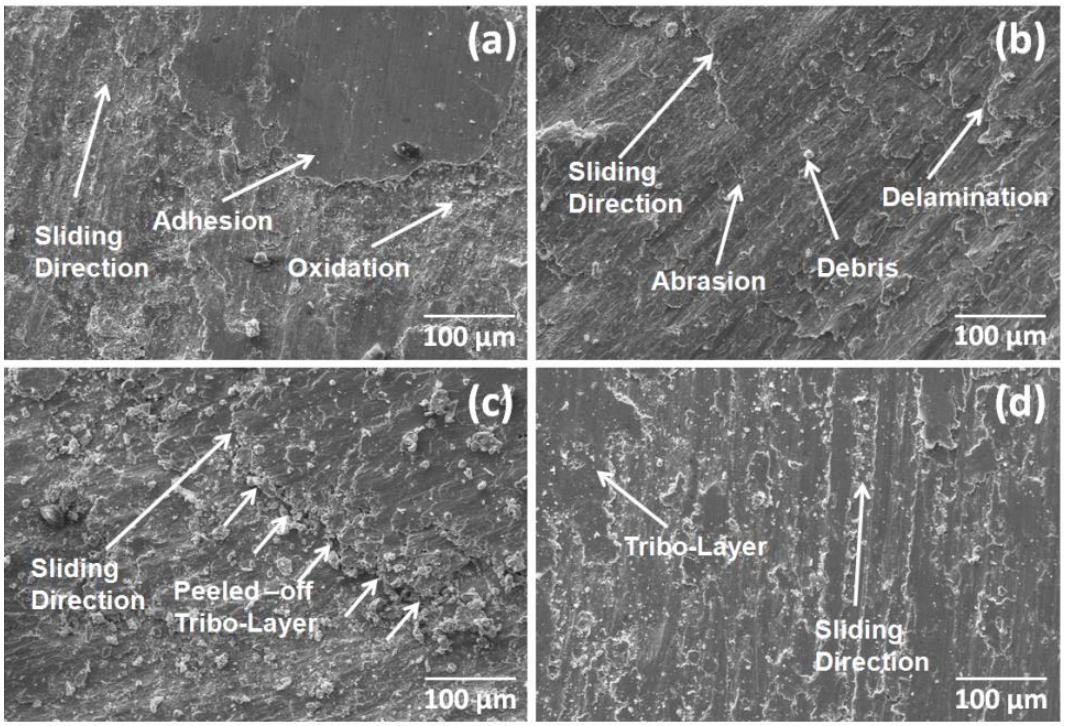

Fig. 6.20 Worn surface micrograph of composites a) CGM 0.5, b) CGM 1.0, c) CGM 1.5, and d) CGM 2.0, tested at the load of 10N and 0.5 m. s^{-1} sliding speed.

Figure 6.21 demonstrates the SEM micrographs of CGM 0.5 and CGM 2.0 composites slid against the EN31 ball at a load of 6 N and speed of 0.5 m. s^{-1} along with their corresponding elemental mapping. SEM micrograph and elemental mapping of the worn surface corresponding to CGM 0.5 composite illustrated in Fig. 6.21 (a) shows the occurrence of adhesion at a few locations whereas, elemental mapping explicitly reveals

the presence of an oxide layer over the worn track. The worn track of CGM 2.0 reflects the presence of a smooth and well compacted tribo-layer as evident from Fig. 6. 21 (b). The elemental mapping of worn surface corresponding to CGM 2.0 nanocomposite (Figure 6.21 b) exhibits a regular distribution of characteristic elements C, O, Mo, and S which indicates that the presence of rGO-MoS_2 in the tribo-layer which is expected to provide lubricity at the interface during sliding.

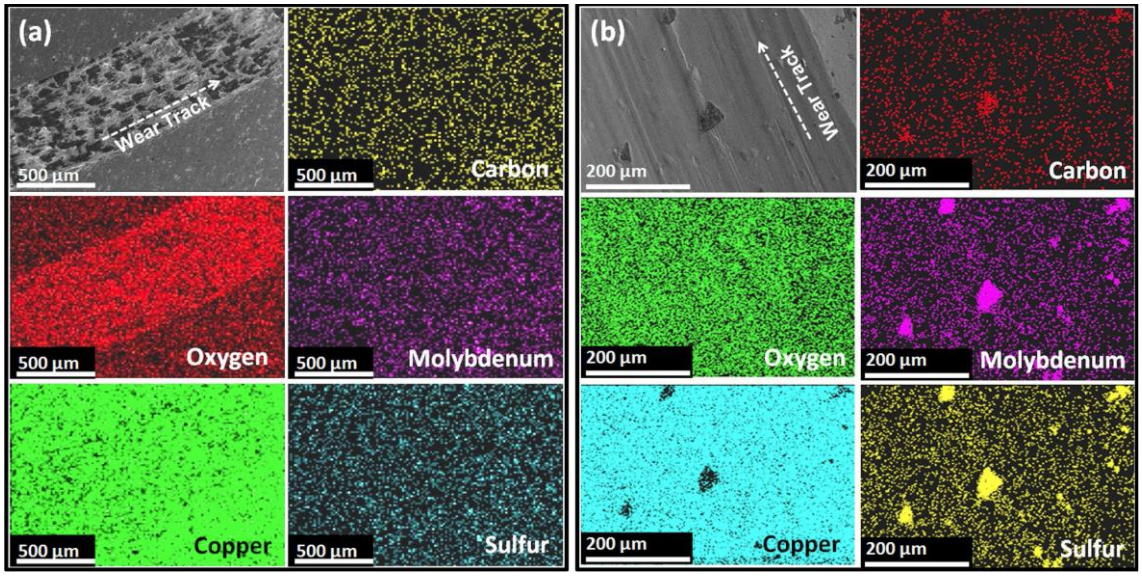

Fig. 6.21 Representative microscopic images and corresponding area elemental distribution of the worn surface of (a) CGM 0.5 and (b) CGM 2.0 nanocomposites at a load of 6N**.**

The worn surfaces of EN31 steel balls slid against the composites CGM0.5, CGM1.0, CGM1.5 and CGM2.0, respectively, at a load of 10 N and 0.5 $m.s^{-1}$ have been examined under SEM to reveal the wear events that the balls might have undergone during sliding which are expected to be helpful in eliciting the possible mechanisms of wear and the possibility of material transfer. Figures 6.22 (a, b) show the low and high magnification micrographs of the worn surface of ball slid against the CGM 0.5 nanocomposite. The low magnification micrograph of the worn surface given in Fig. 6.22 (a) shows a circular worn scar of 1125 µm diameter and displays the sign of adhesion,

which is supported by the presence of transferred material over the worn surface as seen in the high magnification micrograph (Fig. 6.22 b). The worn scar corresponding to CGM 1.0 composite presented in Fig. 6.22 (c) shows an irregular shaped lump formation which has approximately 1350 and 2100 μm of maximum linear and lateral dimensions, respectively. However, the high magnification micrograph given in Fig. 6.22 (d) suggests the occurrence of delamination, probably caused by the brittle fracture. Similar features could be observed for the steel ball slid against CGM 1.5 composite shown in Figs. 6.22 (e and f), however, the lump aggregation is observed to be small in comparison to CGM 1.0. The linear and lateral dimensions for the lump have been found to be 2600 μm and 600 μm. The steel ball slid against the CGM 2.0 composite shows a relatively smooth surface with no measurable signatures of lumps or aggregates as evident from Fig. 6.22 (g, h). One may observe the presence of an oval shaped worn scar with 550 μm minor axis and 720 μm major axis diameter in Fig. 6.22 (g). However, the high magnification micrograph given in Fig. 6.22 (h) reveals some fine abrasive marks along with presence of transfer layer over the counter steel ball surface corresponding to the CGM 2.0.

The morphology of the wear debris collected after the sliding tests has been analyzed under the SEM to explore the nature of wear particles. Fig. 6.23 shows the SEM micrographs of the wear debris generated during the tribo-test at a load of 10 N and 0.5 m. s^{-1}. The wear debris corresponding to CGM0.5 composite shown in Fig. 6.23 (a) has been found to contain some fine as well as larger particles of different shapes. The wear debris pertaining to CGM 1.0 nanocomposite has relatively larger size flakes ranging from hundreds of microns to few mm as evident from Fig. 6.23 (b) whereas that corresponding to CGM 1.5 shown in Fig. 6.23 (c) is a mixture of relatively fine, regular and irregular shaped particles of moderate size as compared to the particle size of CGM1.0. However, the size of particles of the wear debris corresponding to CGM 2.0 are regular in shape with their sizes in the range of few microns.

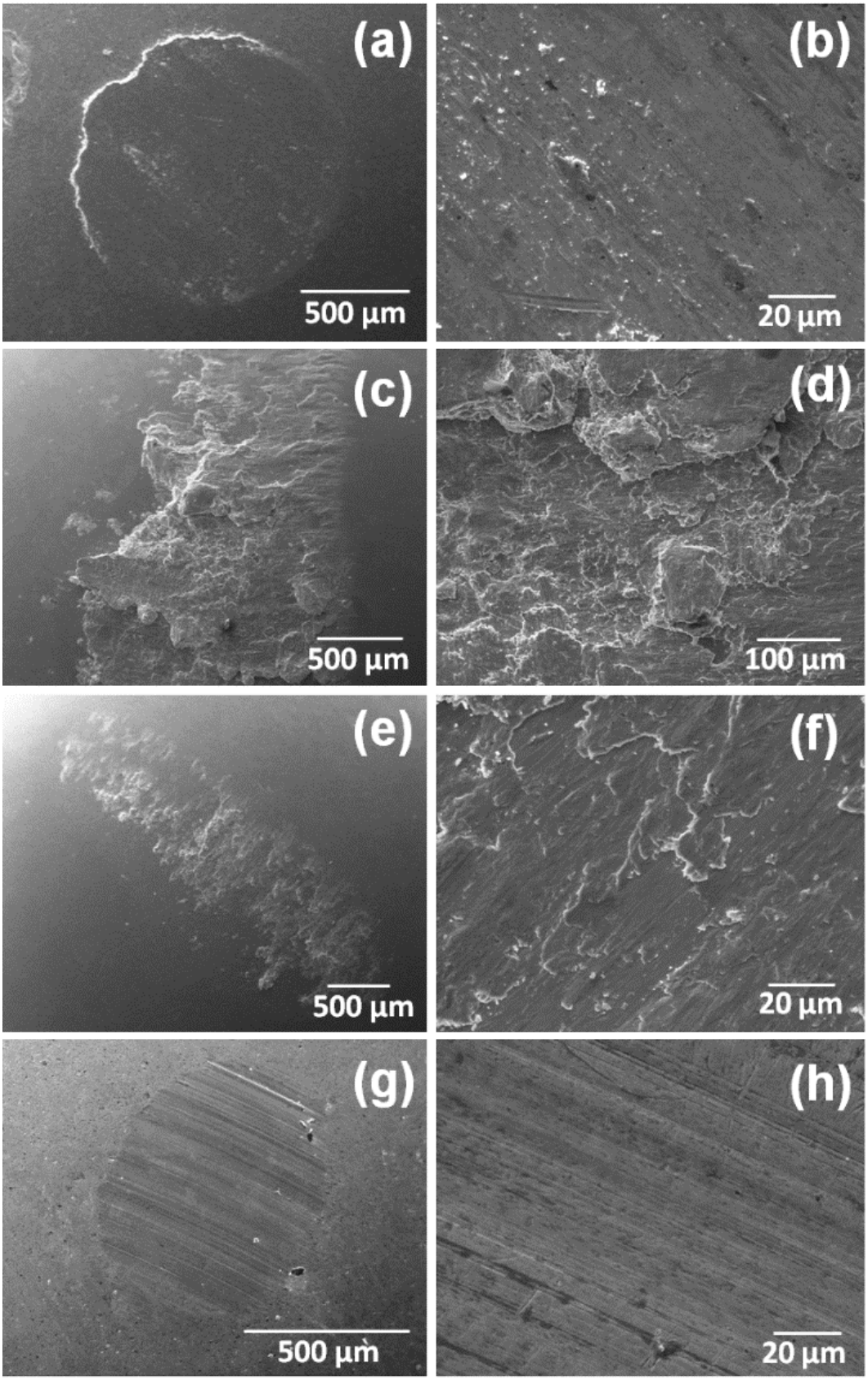

Fig. 6.22 Worn surfaces micrograph of steel balls slid against (a, b) CGM 0.5, (c, d) CGM 1.0, (e, f) CGM 1.5 and (g, h) CGM 2.0 composites shown at low and high resolutions. Load: 10 N, Sliding speed: 0.5 $m.s^{-1}$.

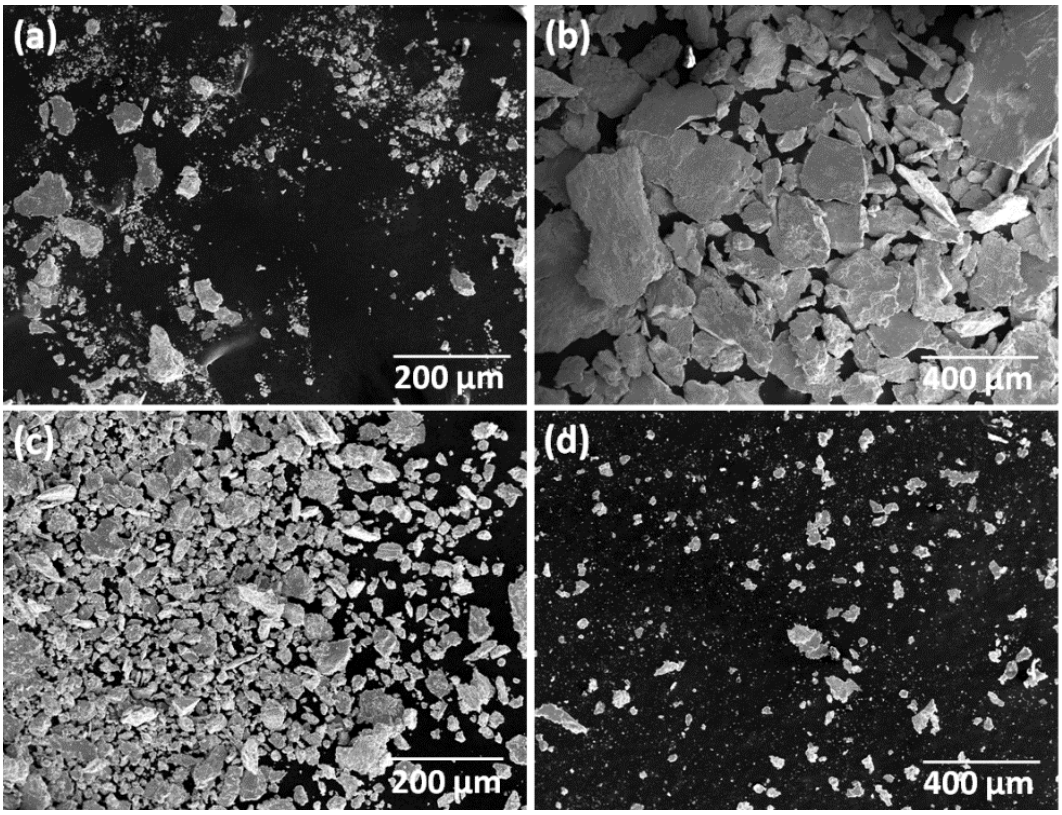

Fig. 6.23 Scanning electron micrographs of the wear debris collected after the tribo-tests for (a) CGM 0.5, (b) CGM 1.0, (c) CGM 1.5 and (d) CGM 2.0 composites slid against the steel ball under the load of 10 N.

6.4 DISCUSSION

Copper based composites containing 0.5, 1.0, 1.5 and 2.0 wt. % rGO-MoS_2 have been synthesized and their mechanical and tribological properties have been presented in the preceding section. Both density and hardness have been found to decrease with increasing content of rGO-MoS_2 in the nanocomposites, except the CGM 0.5 composite as evident from Table 6.2. A relatively lower hardness of CGM 0.5 compared to CGM 1.0 could be attributed to the non-uniform dispersion of reinforced rGO-MoS_2 phase as seen from a comparison of their microstructures given in Figs. 6.2 (a) and (b) which shows agglomeration of reinforced phase in CGM0.5 and an almost uniform distribution in CGM1.0. The agglomeration is considered as an indication of reduction in surface energy of agglomerates occurring due to interfacial interaction and results in pore

formation and lowering of density and hardness as reported earlier by Rajan et al. (2007) also.

This may also explain a relatively lower density of CGM0.5 in comparison to CGM 1.0. The CGM 1.0 nanocomposite has exhibited the highest hardness and density among all composites which may be attributed to the uniform dispersion of the rGO-MoS_2 phase and the formation of MoC which might have also contributed because of being a hard. The decrease in hardness and density beyond 1 wt. % addition of rGO-MoS_2 in composites may attributed to the increase in amount of soft phase (rGO-MoS_2) in the matrix which is supported by the presence of rGO-MoS_2-enriched domains in microscopic images of CGM 2.0 nanocomposite given in Fig. 6.2 (d).

The fluctuating trend of variation of coefficient of friction with number of cycles for copper based composites containing different amounts of rGO-MoS_2 seen from Fig. 6.16 may be attributed to the variation in contact when the specimen and the counter face ball are evolving to develop a better surface conformity. However, amplitude of the fluctuations and average friction coefficient have been found to decrease with increasing rGO-MoS_2 content and this behavior can be explained with the help of worn surface micrographs shown in Figs. 6.19 and 6.20 (a through d). The relatively higher fluctuations and a higher coefficient of friction observed for the composite CGM 0.5 at al the loads may be attributed to the adhesion indicating the possibility of the metal-metal contact between the mating bodies as observed in Figs. 6.19 (a) and 6.20 (a). However, the presence of a tribo-layer on the worn surface of CGM 2.0 may be responsible for a stable and relatively lower coefficient of friction as it impedes metal-metal contact and provides low shearing junctions at the interface. The presence of tribo-layer has been confirmed through SEM micrographs shown in Figs. 6.19 (d) and 6.20 (d) and elemental distribution given in Fig. 6.21 (b).

A slight increase in the average coefficient of friction with increasing load has been observed for all nanocomposites except the CGM 0.5 (Fig. 6.17 a). The increase in the average coefficient of friction could be attributed to the tendency of fragmentation of copper at higher load, which leads to its wearing at sliding interfaces. The wear debris trapped between the sliding interfaces results in increased coefficient of friction, as reported earlier by Raj Kumar et al. (2013). The distinct friction pattern with the function of load shown by CGM 0.5 nanocomposite may be attributed to adhesion. During sliding process, some of wear debris may get ejected because of rotary motion, while the rest get trapped between the sliding surfaces. The ejected debris is direct loss of the material, whereas the trapped one may perform two distinct functions based on the morphology and nature: (a) debris containing hard particles could act as third body abrasives material (b) debris containing soft particles could act as lubricious material and forms a thin tribo film on contact interfaces driven by mechanical action of sliding surfaces. The micrographs of wear debris (Fig. 6.23) suggest that CGM 0.5 and CGM 2.0 nanocomposites yielded relatively fine debris. However, the debris corresponding to CGM 0.5 shown in Fig. 6.23 (a) also contains some larger flake-like particles due to adhesive wear. The fine debris particles observed in Figs. 6.23 (a) and (d) corresponding to CGM 0.5 and CGM 2.0 composite, respectively, are indicative of the mild nature of wear. Therefore, CGM 0.5 and CGM 2.0 nanocomposites exhibit a low wear rate as evident from Fig. 6.18. The degree of compaction and extent of coverage provided by the tribo-layer to underlying material also govern the tribo-performance. A fractured and poorly-compacted transfer layer leads to high adhesion because of the relatively higher possibility of direct metal-metal contact between mating bodies. The broader coverage with the well-compacted tribo layer diminishes the possibility of direct metal-metal contact and improves the tribo-performance. Moreover, the compaction of the transfer

layer depends on the frictional heat generated during sliding, which is governed by sliding conditions, i.e., applied load and speed. The frictional heat is expected to increase with increasing load under the constant sliding speed. The higher friction shown by CGM 0.5 nanocomposite is attributed to adhesion caused by stick and slip phenomenon and presence of a patchy transfer layer with a very less area coverage as seen from Figs.6.19 (a) and 6.20 (a) as compared to that of with CGM 2.0 nanocomposite which shows the presence of a well compacted and smooth tribo-layer over the worn surface as evident from Figs. 6.19 (a) and 6.20 (a). The patchy features of the tribo layer in CGM 0.5 nanocomposite are expected to raise the possibility of metal-metal contact by forming the high shear strength junctions because of the adhesion. This might have led to relatively larger flakes of debris, as seen in Fig. 6.23 (a) corresponding to CGM0.5. The occurrence of material transfer to the counterface ball has been confirmed by SEM micrographs of worn surface of ball given in Figs. 6.21 (a) and (b).

The higher wear rate of CGM 1.0 and CGM 1.5 nanocomposites in comparison to CGM and CGM2.0 may be attributed to two types of abrasions; namely, two-body abrasion because of lump formation at the counterface and the three-body abrasion due to wear particles trapped between the sliding interfaces. The presence of abrasive marks and loose wear particles over the worn surface of CGM1.0 and CGM1.5 further support these abrasive modes as seen from Figs.6.19 (b, c) and 6.20 (b, c). The same may also be confirmed from the worn surface micrographs of the ball slid against CGM1.0 and CGM1.5 and shown in Figs. 6.22 (c to f) which present a rougher surface with signs of delamination caused by brittle fracture. The ductility of nanocomposite is observed to decrease sharply and adhesion events seem to have vanished with increasing rGO-MoS_2 content from 0.5 to 1 wt. %. Moreover, oxide particles also could not form the compact layer due to induced brittleness. The phenomenon may be explained on the

basis of (a) a tribo-layer formation containing lubricating phase, which provides low shear characteristics and is beneficial in reducing the friction and wear and (ii) formation of pores and cracks at matrix/reinforcement interface due to addition of soft phase which deteriorates the mechanical properties which has earlier been reported also by Xiao et. al. (2017). In the present work, non-formation of a compacted transfer layer in CGM 1.0 nanocomposite resulted in loose wear debris particles which probably got trapped between the sliding surfaces and facilitated the third body abrasion. These events might have led to crack propagation and as a consequence to fatigue spalling which could be confirmed by the presence of larger size wear particles on the worn surface of CGM1.0 as evident from Fig. 6.23 (b). However, relatively fine debris particles are observed for CGM 1.5 nanocomposite Fig 6.23 (c) in comparison to those for CGM 1.0 nanocomposite Fig. 6.23 (b) which may be attributed to the formation of the tribo layer during the initial sliding of CGM 1.5 nanocomposite. The higher coefficient of friction ($\mu = 0.8$) after certain cyclic contacts as seen from Fig. 6.16 could be attributed to peeling off of the tribo-layer which is observed in the worn surface micrographs of CGM1.5 given in Figs.6.19 (c) and 6.20 (c).

The effect of load on the friction and wear behavior of Cu-rGO-MoS_2 composites having different amounts of rGO-MoS_2 has been examined by conducting tests under different loads of load of 4, 6, 8 and 10 N. No significant changes are observed in coefficient of friction with increasing load for all the composites as seen from Fig. 6.17 (a).The observed behavior may be explained on the basis of SEM micrographs of the worn surfaces of the composites slid at the lowest (4 N) and the highest (10 N) loads used in the present study presented as Figs. 6.19 (a through d) and 6.20 (a through d) which present almost similar morphology with the change in load like the SEM micrographs of CGM 0.5 at 4 and 10 N load shown in Figs. 6.19 (a) and 6.20 (a) exhibit the adhesion and

oxidation as the major wear mechanisms. Similar explanation may also suffice for other composites, namely. CGM1.0, CGM1.5 and CGM2.0 as no change in worn surface morphology could be observed for each at 4 and 10 N as evident from Figs. 6.19 (b, c, d) and 6.20 (b, c, d). As far as wear rate is concerned, no measurable changes have been observed in the wear rate of the composites CGM0.5 and CGM2.0 with increasing load from 4 to 10 N. However, the wear rate for CGM1.0 and CGM1.5 has been observed to increase with increasing load as seen from Fig. 6.18 (a) which is not surprising as wear rate is generally found to increase with load (Sun et al., 2019). The increase in wear rate with load may be explained on the basis of SEM micrographs of the worn surface of CGM1.0 and CGM1.5 shown in Figs. 6.19 (b, c) and 6.20 (b, c) which indicate abrasion along with the peeling off of the transfer layer resulting in more possibility of direct metal-metal contact in these composites and consequently, a higher loss of material. The severity of abrasion and peeling off of the transfer layer have been observed to be more at a load of 10 N in comparison to 4 N which can be judged from a comparison of Figs. 6.17 (b) and 6.18 (b) for CGM1.0 and Figs. 6.17 (c) and 6.18 (c) for CGM1.5 which may explain an increase in wear rate with load for CGM1.0 and CGM1.5. However, no significant change in wear rate with respect to load is observed for CGM0.5 as seen from Fig. 6.18 (a). The SEM micrographs of the worn surface of CGM0.5 shown in Figs. 6.19 (a) and 6.20 (a) at the loads of 4 and 10 N, respectively, show the presence of adhesive features and oxide layer with almost similar nature at both the loads. The elemental mapping of the worn surface of CGM 0.5 composite slid under a load of 6 N and shown in Fig. 6.21 (a) confirms the presence of an oxide layer over the wear track this layer protects the underlying material from direct metal-metal contact and reduces wear resulting in relatively fine wear debris particles as evident from Fig. 6.23 (a). As far as composite CGM 2.0 is concerned, a marginal increase in wear rate is observed with increasing load as evident from Fig. 6.18 (a). At a load of 4 N a smooth and compacted

tribo-layer is seen over the worn surfaces of CGM 2.0 along composite (Fig. 6.19 d) along fine abrasive marks whereas minor delamination along with a compacted tribo-layer is observed on the surface worn at 10 N (Fig.6.20 d). The elemental mapping of worn surface corresponding to CGM 2.0 shown in Fig 6.21 (b) composite has confirmed the formation of a tribo-layer consisting of carbon, MoS_2 and oxides which might have provided low shearing junction at the interface along with inhibiting metal-metal contact resulting in lower wear rate. A marginal increase in wear rate with load may be attributed to the increased possibility of penetration of the tribo-layer by the counterface asperities at relatively higher loads.

The prevailing mechanism of wear for CGM 0.5 is observed to be a combination of adhesion and oxidation under the range of loads used in the present study, whereas the same for CGM 1.0 is a mix of delamination and two/three body abrasion. The wear mechanism observed for Composite CGM 1.5 is a combination of two and three body abrasion, while the same for composite CGM 2.0 is mild abrasion.

Fig. 6.24 illustrates the plausible wear mechanism for nanocomposites emphasizing the role of rGO-MoS_2 nanofiller based on the results of friction and wear and microscopic images of the worn surface along with elemental distribution. The CGM 0.5 nanocomposite exhibits rGO-MoS_2 filler as an agglomerated phase in the copper matrix (Fig. 6.2 a) and yields less amount of wear debris. The hard oxide layer formed over the surface of CGM 0.5 nanocomposite during friction test prevents further wearing of the surface (Fig. 6.20). However, several adhesion sites seen over the worn track in the form of patches could be due to retained ductility of material at low reinforcement content which encourages wear debris material to adhere to the surface with stick-slip characteristics. Therefore, relatively higher friction but low wear rate has been observed for CGM 0.5 nanocomposite (Fig. 6.16 to 6.18). The relatively higher dosage (1 wt. %)

of rGO-MoS_2 in the CGM 1.0 nanocomposite furnishes good interaction between rGO-MoS_2 and Cu matrix leading to an increase in hardness and simultaneous inducement of brittleness in the material. The higher brittleness helps in propagation of the cracks in the oxide layer formed during the sliding process resulting in the detachment of hard and brittle debris particles from the contact interface of CGM 1.0 nanocomposite. The release of these worn particles from the sliding interfaces increases the wear rate, in spite of the higher amount of lubricant filler (rGO-MoS_2). Over the number of cyclic contacts, these abrasive particles get compacted and adhere to counterface resulting in the formation of a hard lump at the counterface due to strain hardening, which may lead to two-body abrasion. As the amount of reinforcement phase, i.e., rGO-MoS_2 is increased to 1.5 wt. % (CGM 1.5 nanocomposite), more fraction of rGO-MoS_2 is available to extend the lubrication properties of nanocomposite. As the sliding initiates, tribo layer formation occurs over the worn surface, however, after a few cycles tribo-layer gets peeled off by the abrasive action of third body particles. However, the rGO-MoS_2 rich surface favors the smooth sliding and forms the rGO-MoS_2 enriched tribo-layer at the contact interfaces. Since the amount of reinforcement is not sufficient to provide a continuous tribo-layer; hence, the lubricating effect is able to sustain only for a finite number of cycles. The diminution of tribo-layer starts with the interaction of wear particles between the mating surfaces. The increase in interaction of worn particles with mating surfaces leads to peeling-off of the tribo-layer and results in a sharp rise in coefficient of friction (Fig. 6.16). The CGM 2.0 nanocomposite containing the highest amount of 2 wt. % of rGO-MoS_2 filler forms a well compacted rGO-MoS_2 enriched tribo-layer as seen in Fig. 6.21(d), which provides a low shearing strength film at the interface and results in both low friction and wear rate.

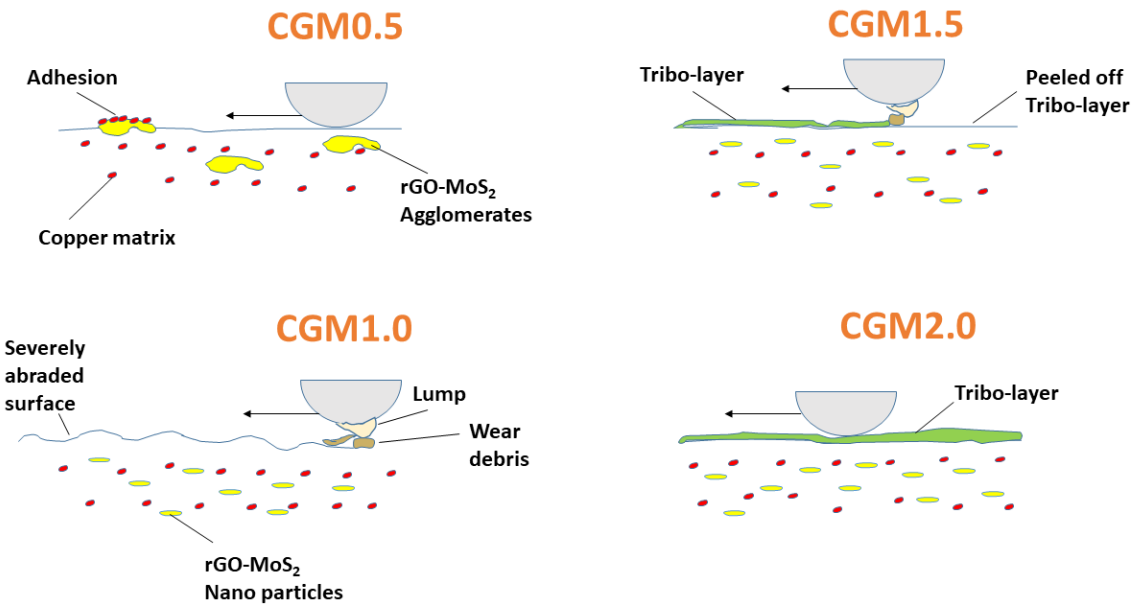

Fig. 6.24 Schematic illustration depicting the plausible wear mechanism of Cu-rGO-MoS_2 nanocomposite, emphasizing the role of rGO-MoS_2 nanofiller.

Based on the results and discussion presented above it can be inferred that Cu-rGO-MoS_2 composites reinforced by different rGO-MoS_2 content (0.5 to 2 wt. %) and synthesized by spark plasma sintering at 700 ^{0}C, density and hardness of Cu-rGO-MoS_2 nanocomposites decreases with increasing content of soft and low-density rGO-MoS_2 phase except for the composite containing 0.5 wt. % rGO-MoS_2. This has been attributed to the non-uniform distribution of the reinforcing phase. A relatively higher coefficient of friction shown by the composites having 0.5 and 1 wt. % rGO-MoS_2, namely, CGM0.5 and CGM1.0, has been attributed to the high adhesion and two/three-body abrasion. An increase in the rGO-MoS_2 content up to 1.5 wt. % results in lowering of coefficient of friction (~ 0.2) during initial cycles due to tribo-layer formation, which eventually shoots up to (~ 0.65) due to peeling off the tribo-layer by third body abrasion. The CGM 2.0 composite having a relatively higher amount (2 wt. %) of rGO-MoS_2 nanofiller is able to provide low friction ($\mu = 0.2$) with a low wear rate due to the formation of well-compacted lubricious tribo layer at the sliding surface. Among all samples, CGM 2.0 nanocomposite containing 2.0 wt. % rGO-MoS_2 exhibits the lowest friction and wear. The results indicate

that rGO-MoS_2 has the potential to be used as solid lubricating filler in the metal matrix composites for the enhancement of tribological properties.